40

Nonlinear (Harmonic Generation) Optical Microscopy

Ping-Chin Cheng and C.K. Sun

INTRODUCTION

In recent years, light microscopy, particularly fluorescence microscopy, has been extensively useful in the study of living cells and tissues. Although it has become an important tool in biological research, both single- (Sheppard and Shotton, 1997) or two-photon (Denk *et al.*, 1990; Cheng *et al.*, 1998, 2001) excitation schemes require that the specimen contain either intrinsic or extrinsic fluorescent probes. These probes include fluorescent dyes, fluorescent proteins, and quantum dots and common problems include probe penetration, probe toxicity, and photobleaching/damage (Konig, 1995; Cheng *et al.*, 2001a). To be useful, the fluorescent probes must usually be bound to specific biostructures or molecules, either by partition of the dye into various compartments, antigen–antibody reactions, affinity or site-specific binding of dye(s), or the transgenic expression of fluorescent and luminescent proteins. In addition, the probe may interact with the ionic environment to give a specific fluorescence signature. In all these cases, the fluorescence signals are related to the chemistry of the dye and the chemistry of the interaction between the dye and the cell or tissue or the genetic expression of the probe. Therefore, the term "chemical" and "biochemical" contrast is frequently used to describe the fluorescence imaging modality.

On the other hand, nonlinear imaging modalities exist that create contrast based on the organization and orientation of nanostructures in the specimen, and these can often provide an alternative tool for studying the dynamics of cellular structures and functions. These nonlinear imaging modalities include second and third harmonic generation (SHG and THG), in which specific structural features of the optical configuration of the native specimen generate prompt signals. In this case, signal is generated by nonlinearity in the physical properties of the specimen (such as short-period modulations or discontinuities in its refractive index, RI) particularly those that occur at very high excitation intensity, such as that present at the focus point of an objective lens illuminated with high-intensity, femtosecond pulsed laser. Unlike fluorescence, these harmonic signals are generated with no time delay at all and emerge at wavelenghts that are exact integer submultiples of the excitation wavelength and traveling in the same direction (forward).

Recent studies on man-made nanoperiodic structures (e.g., super-lattices) indicate a strong enhancement in SHG when high-intensity light is incident on non–centri-symmetric structures (Zhao *et al.*, 1999; Kao *et al.*, 2000; Sun *et al.*, 2000). SHG occurs because the structure violates the condition of optical centro-symmetry. This sort of breakdown occurs in the inorganic crystals used for doubling the frequency of laser light (see Chapter 5, *this volume*). A typical application is the frequency doubling of 1064 nm emission from a semiconductor laser to produce the 532 nm light in the green-laser pointer. More generally, SHG occurs in many other structured samples, some of which are biological.

A super-lattice structure is basically a one-dimensional nonlinear $\chi^{(2)}$ photonic crystal (where $\chi^{(2)}$ is the second-order nonlinear susceptibility), which is defined as a material with a periodicity in its second-order nonlinear dielectric properties (Berger, 1998). Strong SHG-enhancement has also been reported in one-dimensional and two-dimensional nonlinear photonic crystals (Broderick *et al.*, 2000; Dumeige *et al.*, 2001). The mechanism is similar to the bandgap-resonant enhancement that occurs in common SHG-conversion crystals and, although SHG conversion efficiency is always highest near the nonlinear photonic bandgap, it does not vanish even when the illumination (pump) wavelength is far away from the spatial modulation period (the bandgap). Quasi–phase-matching is an example of this, as the operating wavelength of the excitation is much shorter than the spatial modulation period of the nonlinear coefficient $\chi^{(2)}$. Recently, strong SHG has been reported in several types of biological material, mainly in orderly packed biomolecules or macromolecular structures (Chu *et al.*, 2001; Cheng *et al.*, 2002; Sun *et al.*, 2003). In contrast, no SHG occurs in amorphous materials, such as the almost randomly arranged macromolecules and other nanostructures that make up a cell.

The enhancement of SHG by the nanophotonic crystals of the membrane protein bacteriorhodopsin (bR), has recently been demonstrated using hyper-Rayleigh scattering (Clays *et al.*, 2001). The bR protein forms a two-dimensional (2D) crystal in the purple membrane of *Halobacterium salinarium* (Birge *et al.*, 1990). This structure has an alternating change in second-order nonlinearity with a ~5 nm period, causing it to act as a nonlinear photonic crystal (Berger, 1998). A number of other highly organized biological nanostructures have been reported that appear to break optical centro-symmetry and behave as SHG-active nonlinear photonic crystals. Such structures include stacked membranes such as those found in the myelin sheath, the endoplasmic reticulum (ER), the Golgi apparatus, and the grana in the chloroplast, microtubules, cellulosic microfibrils, collagen fibers, enamel prisms, bone matrix, starch granules, and mineral deposits in plants (Chu *et al.*, 2001; Cheng *et al.*, 2002; Sun *et al.*, 2003, 2004). Similar to the backward SHG and THG detected in a waveguide, Gu and colleagues (1999) and Sun and co-workers (2005) reported strong backward SHG from microtubules, a fact that allows imaging the cytoskeleton and the mitotic spindle in living tissue.

Collagen, the major protein of the extracellular matrix, is one of the best-known SHG structures in biology. The collagen mole-

Ping-Chin Cheng • State University of New York, Buffalo, New York 14260, and National University of Singapore, Singapore
C.K. Sun • National Taiwan University, Taipei, Taiwan, Republic of China

Handbook of Biological Confocal Microscopy, Third Edition, edited by James B. Pawley, Springer Science+Business Media, LLC, New York, 2006.

cule is a long, stiff, triple-stranded helical structure, in which three collagen polypeptide chains, called α-chains, are wound around one another in a ropelike superhelix. After being secreted into the extracellular space, these collagen molecules assemble into high-order polymers called collagen fibrils that are 10 to 300 nm in diameter and many hundreds of micrometers long. Collagen fibrils often aggregate into larger, cable-like bundles, several micrometers in diameter, which can be seen in the light microscope as collagen fibers. Under electron microscopy, collagen fibrils have characteristic cross-striations every 67 nm, reflecting the regularly staggered packing of the individual collagen molecules in the fibril. This regularly staggered packing order provides the needed structural condition for efficient SHG (Williams *et al.*, 2005; Sun *et al.*, 2004).

The SHG signal is created in proportion to the square of the instantaneous local intensity (Gannaway and Sheppard, 1978). As a result, like two-photon fluorescence (2PF) microscopy (Denk *et al.*, 1990; Cheng *et al.*, 1998), SHG provides intrinsic axial resolution. SHG microscopy was first demonstrated in studies of SHG photonic crystals (Gannaway and Sheppard, 1978), surfaces/interfaces (Shen, 1989), electric field distribution in semiconductors (Sun *et al.*, 2001), and was also shown to be present in studies of tissue polarity (Freund *et al.*, 1986; Guo *et al.*, 1997) and of membrane potentials in cells (Campagnola *et al.*, 1999; Peleg *et al.*, 1999; Moreaux *et al.*, 2000b).

Because most biological structures are not highly ordered, they are optically isotropic and do not produce any SHG signal. Only those few biological structures that are ordered or that involve some spatial organization that breaks the optical centro-symmetry can produce harmonic signals. In contrast to fluorescence processes that involve the excitation of the fluorescent molecule to an excited state having a finite lifetime, harmonically generated signals involve only virtual states that involve no time delay. The marked advantage of this virtual transition is the lack of energy deposition in the specimen. As a result, SHG produces no photodamage or bleaching, and like backscattered light, can be regarded as a truly "non-invasive" imaging modality. However, it is important to remember that the very high instantaneous power levels required to produce the effect may cause other novel and damaging nonlinear damage mechanisms to occur (see Chapter 38, *this volume*). As both harmonic generation and nonlinear absorption processes can occur simultaneously, it is also possible to produce photodamage due to absorption processes if absorbers are present. In fact, as some small amount of nonlinear absorption always occurs in biological specimens, the main advantages of SHG are not just that the signal generation process involves no energy deposition, but that it provides specific structural information. In contrast to the chemical specificity that characterizes fluorescence imaging, harmonic generation (SHG and THG) provides an imaging modality specific for structural configuration.

Discontinuities in RI or the optical dispersion properties of biological tissues can generate third harmonic generation (THG) signals (Barad *et al.*, 1997; Muller *et al.*, 1998; Moreaux *et al.*, 2000a,b; Sun *et al.*, 2001) and the intensity of these signals is proportional to the third power of the illumination intensity. Using the same illumination wavelength, THG provides even better optical-sectioning resolution than SHG or 2PF, but is also more sensitive to changes in the intensity of the light in the focused spot, such as those caused by laser instability or by scattering or defocusing of the illumination. The THG can be used to study optical interfaces in the cell such as those at cell membranes or organelle surfaces. For example, the surface of the erythrocyte can generate significant THG (Sun *et al.*, 2004).

HARMONIC GENERATION

Shortly after the first demonstration of the laser by Maiman in 1960, the next year Franken and co-workers discovered the process of SHG in man-made materials. This work is often taken as the beginning of the field of nonlinear optics. Nonlinear optical phenomena are "nonlinear" in the sense that they occur when the response of a specimen depends upon the strength of the optical electric field in a nonlinear manner. For example, SHG occurs as a result of that part of the atomic response to the oscillating field of the light that depends quadratically on the strength of this optical field. Consequently, the intensity of the signal generated by the SHG mechanism increases as the square of the intensity of the incident light. By the same token, THG signals vary with the cube of the intensity of the incident light.

An image is a two-dimensional recording of the interaction between light and a specimen, and therefore is a representation of the optical properties of the specimen. In conventional optical imaging, contrast mechanisms include interactions such as absorption, reflection, scattering, and fluorescence, and the response recorded is linearly dependent on the intensity of the incident light. In the nonlinear optical domain, high-intensity light causes a variety of "anomalous" optical responses, and therefore the image contrast mechanism represents not only the differences in optical properties of the specimen, but also the result of the modification of those optical properties that depend on the intensity of the light in a nonlinear manner. In the case of conventional (linear) optics, a linear relationship exists between the electric field strength of the light and the induced polarization of the object. At relatively low incident intensity, the optical response can be approximated to be the first-order response as:

$$\tilde{P}(t) = \varepsilon_0 \chi^{(1)} \tilde{E}(t) \tag{1}$$

where $\chi^{(1)}$ is the linear susceptibility, $\tilde{P}(t)$ is the dipole moment per unit volume, or polarization of a material system, $\tilde{E}(t)$ is the strength of an applied optical field, and ω is the frequency.

Second Harmonic Generation

In contrast, at high incident intensity, the nonlinear optical response can be described by:

$$\begin{aligned}\tilde{P}(t) &= \varepsilon_0 \chi^{(1)} \tilde{E}(t) + \varepsilon_0 \chi^{(2)} \tilde{E}(t)^2 + \varepsilon_0 \chi^{(3)} \tilde{E}(t)^3 + \ldots \\ &\equiv \tilde{P}^{(1)}(t) + \tilde{P}^{(2)}(t) + \tilde{P}^{(3)}(t) + \ldots\end{aligned} \tag{2}$$

where $\chi^{(2)}$ is the second-order nonlinear susceptibility and $\chi^{(3)}$ is the third-order nonlinear susceptibility.

In the above equation, because the fields are vectors, the nonlinear susceptibilities are tensors. As each atom acts as an oscillating dipole that radiates in a dipole radiation pattern, the radiation phase among the enormous number of atoms must be matched to induce constructive interference and thus nonlinear generation is allowed under phase-matching conditions (i.e., when the scattered light **is** in phase). This leads to the generation of radiation at the second harmonic frequency (half the wavelength of the illumination). However, this situation does not lead to the generation of electromagnetic radiation because its second time derivative vanishes and a static electric field is created within the nonlinear crystal.

Second harmonic generation can also be considered as an interaction involving the exchange of photons between the various frequency components of the field. In SHG, two photons of frequency ω are destroyed and one photon of frequency 2ω is simultaneously created in a single quantum-mechanical process. The

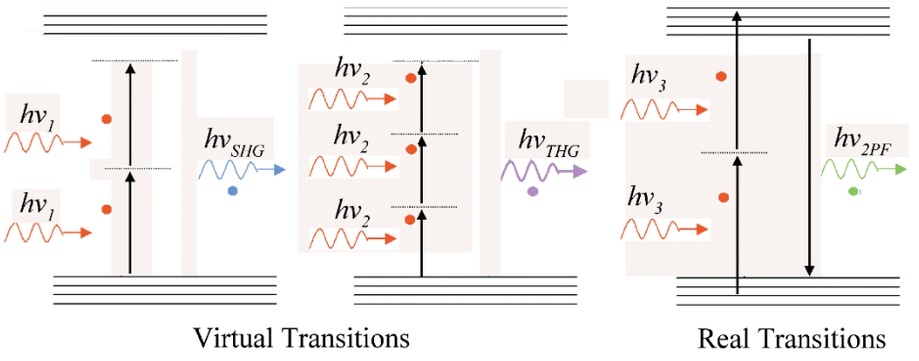

FIGURE 40.1. Energy state diagram. Both SHG and THG involve virtual transitions in which no energy is absorbed by the specimen. In contrast, two-photon fluorescence (2PF) involves the absorption of energy (real transitions) and excitation of molecules. The wavelength of SHG is half and THG is one third that of the incident wavelength, while 2PF has an emission wavelength more than half of the incident wavelength.

solid lines in Figure 40.1 represent the atomic ground states, and the dashed lines represent virtual levels. These levels are not energy eigenlevels of the free atom, but rather represent the combined energy of one of the energy eigenstates of the atom and of one or more photons of the radiation field.

The fact that SHG vanishes in any material system that possesses centro-symmetry (i.e., one that has a center of inversion) can be explained by changing the sign of the applied electric field in Eq. 2. In a medium possessing inversion symmetry, the sign of the induced polarization must also change. Hence, relation 2 is replaced by

$$-\tilde{p}^{(2)}(t) = \varepsilon_0\chi^{(2)}[-\tilde{E}(t)]^2 = \varepsilon_0\chi^{(2)}\tilde{E}(t)^2 \qquad \textbf{(3)}$$

By comparing Eq. 3 with Eq. 2, $\tilde{P}(t)$ must equal $-\tilde{P}(t)$, and this can occur only if $\tilde{P}(t)$ vanishes identically. So $\chi^{(2)}$ is equal to zero for centro-symmetric media and no SHG signal is expected. Because the molecules making up most biological materials are oriented more or less "at random" (compared to a crystal, for example), they generate no SHG signals. The phase-matching condition in SHG is that the wave vector difference between input excitation light and output harmonic light is zero. Therefore, phase-matching is seriously affected by polarization, and SHG is sensitive to the angle between the polarization of the incident light and the symmetry condition of the material. Pol-dependent SHG can provide information about crystal orientation and imperfection, macromolecular structure and orientation, and regions where the centro-symmetry either breaks down, such as at surfaces and optical interfaces or where it is induced by organized, submicron structures. It can also be created by large localized residual electric fields, such as those across electrically polarized cell membranes.

Third Harmonic Generation

Third harmonic generation involves a process whereby three photons of frequency ω are destroyed and one photon of frequency 3ω is created. A nonlinear contribution to the polarization of the medium at the frequency of the incident field leads to a nonlinear contribution to the refractive index experienced by a wave at frequency ω.

Normally, the tightly focused condition in a microscope setup inhibits the production of third harmonic signals (Barad *et al.*, 1997; Berger, 1998), and a positive wave vector ($\Delta k = 3k_\omega - k_{3\omega} > 0$) mismatch between the fundamental and harmonic beam is required to achieve phase-matching. Under tight focusing conditions, third harmonic production is allowed if an optical interface is present within the focal volume, no mismatch is required, and the resulting breakdown in focal volume symmetry enables efficient THG generation for $\Delta k < 0$ (normal dispersion).

When one calculates the third harmonic power as a function of the interface uniformity, there is a change in either the refractive index or in the third-order nonlinear susceptibility, and this has the result that the third harmonic power does not vanish. Barad and colleagues (1997) demonstrated that, as a result of this interface effect, imaging with the third harmonic is possible and is especially suitable for transparent phase specimens with low intrinsic contrast such as the cell boundary. The THG signal strength is sensitive to changes in the nonlinear optical properties of the specimen.

Multi-Photon Absorption and Fluorescence

Because in 2PF, the absorbed power is proportional to the square of the incident light intensity (i.e., as if it depended on the square of the photon concentration), this process is called two-photon absorption. The absorbed two-photon energy can excite a molecule to its excited state or even to ionization (two-photon ionization). In the process of two-photon fluorescence, an atom/molecule makes a transition from its ground state (S_0) to a real excited state (S_2) by the simultaneous absorption of two laser photons and quickly transits to a metastable state (S_1) and then emits one photon with higher frequency (ν_{em} but less than $2\nu_{ex}$) while returning to the ground state ($S_1 \rightarrow S_0$). The transition between the first excited state and the metastable state can produce chemical events that lead to photobleaching, a process that removes the fluorescent species from the fluorescing pool (see Chapter 39, *this volume*). Moreover, the excess absorbed energy that is lost as vibrational energy during the transition, can result in photodamage, and this process may become even worse as the energy difference between these two states increases.

LIGHT SOURCES AND DETECTORS FOR SECOND HARMONIC GENERATION AND THIRD HARMONIC GENERATION IMAGING

Because SHG and THG signal strength is quadratically or third-power dependent on the intensity of the illumination, high illumination intensity is required for the efficient generation of these signals. As continuous illumination (CW) at such high intensity would result in unacceptably high energy deposition, one instead uses the high instantaneous power density that can be achieved using a mode-locked, ultra-fast pulsed laser. Four such laser systems (Table 40.1) are currently available for use in nonlinear microscopy: the titanium:sapphire (Ti:Sa) (various suppliers), the Cr:forsterite laser (Avista Project, Russia; Ming-mei Technology, Taiwan, Republic of China), the Nd:glass laser (Time-Bandwidth Products, Switzerland), and the femtosecond ytterbium laser (Amplitude System, Talence, France).

The Ti:Sa has a tuning range of about 700 to 980 nm [near-infrared (NIR)] and is currently used extensively in two-photon fluorescence microscopy. The SHG wavelength excited by a Ti:Sa femtosecond laser operating at 810 nm will be in the deep blue at 405 nm, while 2PF will be in the visible region (>405 nm). However, the THG signal generated by a 810 nm primary beam will fall at 270 nm, in the deep ultraviolet (UV) region, while three-photon fluorescence (3PF) will be found at >270 nm. Consequently, the THG and 3PF signals will suffer from the high UV absorption of most biological specimens (Fig. 40.2; Cheng *et al.*, 2001a; Lin *et al.*, 2001), making signal detection difficult. In addition, one would need special (and expensive!) UV objectives, mirrors and photomultiplier tubes (PMT) in the detecting path.

In contrast, the Cr:forsterite laser operates in the range of 1230 to 1270 nm in the IR spectrum, making it an excellent light source for multi-modality microscopy (Bouma *et al.*, 1996; Chu *et al.*, 2002). For example, operating a Cr:forsterite laser at 1230 nm allows SHG (615 nm), THG (410 nm), 2PF (>615 nm), and 3PF (>410 nm), all to fall within the visible spectrum. In addition, the lowest light attenuation in biological material is generally found in the 1000 to 1300 nm range (Fig. 40.2). By moving the excitation wavelength to 1230 nm, not only the visible but also the NIR spectrum is open for signal recording. This could be important in imaging botanical specimens that have a high autofluorescence output over nearly the entire visible spectrum (see Fig. 20.2, *this volume*). The fact that autofluorescence diminishes at wavelengths longer than the fluorescence emission of chlorophylls makes NIR fluorescent probes, such as AlexaFluor 750, Cy5.5 and Cy7 (Molecular Probes Inc., Eugene, OR), very attractive. Development of endogenous fluorophore mutants (i.e., long-wavelength fluorescent proteins) having emission wavelengths longer than DsRed will be helpful for the study of botanical specimens. Liu and colleagues (2001) and Cheng and co-workers (2001) have demonstrated that a number of commonly used fluorescent probes can be efficiently excited at 1230 nm by 2PF and 3PF.

On the other hand, mode-locked femtosecond Nd:glass and diode-pumped ytterbium lasers provide an alternative choice. A typical femtosecond Nd:glass system offers a tuning range of 1053 to 1064 nm, with a repetition rate of 70 to 150 MHz and a 150fs pulse width (Time-Bandwidth Products, Zurich). This laser will produce SHG signal at 526 to 532 nm, which is at the second attenuation minimum of green botanical specimens (Fig. 40.2). The

TABLE 40.1. Pulsed Lasers Suitable for Generating SHG and THG Signals

Laser System	Wavelength Range (nm)	Pulse Width (fs)	Repetition Rate (Hz)
Ti:Sa	700–980	100	76–100 MHz 2 GHz, Chu *et al.*, 2003b
Nd:glass	1053–1064	150	70–150 MHz
Cr:forsterite	1230–1270	65	76–120 MHz
Diode-pumped ytterbium	1030	200	50 MHz

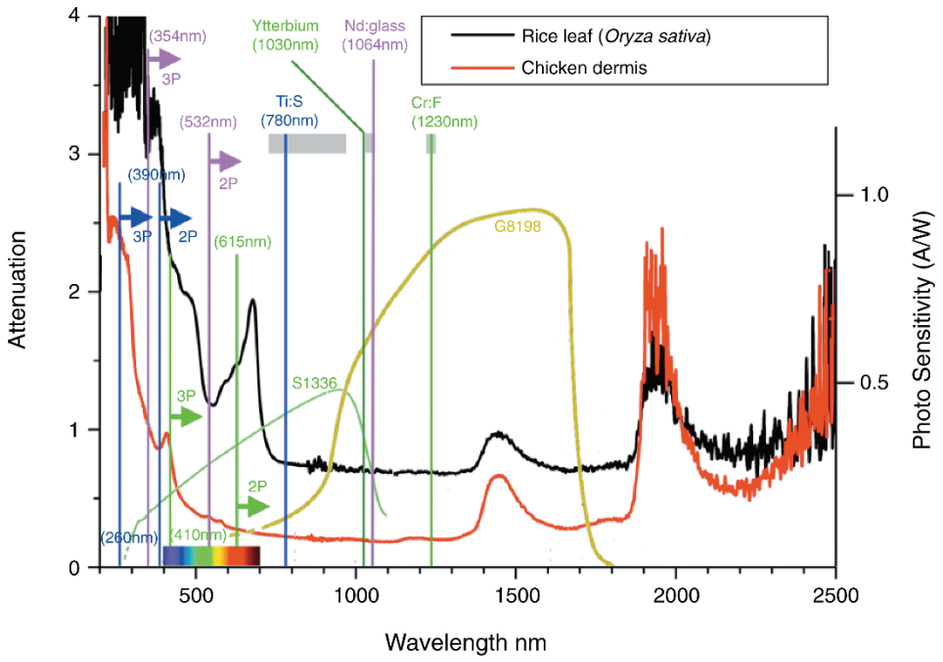

FIGURE 40.2. Light attenuation spectra (absorption and scattering) in rice leaf (*Oryza sativa*) and chicken dermis. Note the operating ranges of Ti:Sa, ytterbium, Nd:glass, and Cr:Forsterite lasers. The light green lines indicate a typical emission wavelength of Cr:Forsterite (1230 nm) and its corresponding SHG (615 nm) and THG (410 nm). The blue lines represent a typical Ti:Sa emission wavelength (780 nm) and the corresponding SHG (390 nm) and THG (260 nm) wavelengths. The purple lines indicate the emission line of Nd:glass and corresponding SHG (532 nm) and THG (352 nm) lines. The dark green line indicates the emission line of ytterbium laser (1030 nm). The curves labeled S1336 and G8198 represent the sensitivity of typical visible and NIR photodiode detectors.

THG is situated at 351 to 354 nm. Because both the excitation and emission wavelength are optimized at an attenuation minimum, using Nd:glass greatly increases the imaging depth in tissue, particularly green plant tissue. Using this laser system, one can obtain useful 3PF, 2PF, and SHG simultaneously and it has the added advantage that many commercially available IR objectives have reasonable transmittance at the 1064 nm wavelength. On the other hand, the diode-pumped ytterbium laser operates at 1030 nm, with SHG and THG at 515 nm and 343 nm, respectively.

Figure 40.2 summarizes the operating wavelengths and the SHG and THG signals of the four mode-locked ultra-fast lasers in reference to the attenuation spectra of biological specimens and detector sensitivity. In the near UV wavelength region, attenuation is dominated by the strong absorption of common tissue constituents such as proteins and carbohydrates. For IR wavelengths longer than 1400 nm, however, the molecular resonance absorption of water starts to dominate the attenuation. As a result, biological specimens have a relatively transparent window between 350 to 1300 nm.

Although the Ti:Sa laser, operating at around 720–950 nm, has been widely adopted as the preferred light source for multi-photon microscopy, one can easily see that the attenuation minimum is around 1000 to 1300 nm, not in the Ti:Sa range. In fact, this should not be surprising because scattering cross-sections become smaller as the wavelength increases. This plot is also in good agreement with previous measurements of the attenuation coefficients of biological materials such as human skin (Anderson and Parrish, 1981), maize stem (Cheng *et al.*, 1998), and leaves (Lin *et al.*, 2001).

The advantage of the Ti:Sa laser is its large tuning range compared to the Cr:forsterite and Nd:glass lasers. In addition, while most objective lenses work well in the NIR spectrum (up to 900 nm) and some IR objectives have reasonable transmission up to ~1100 nm, obtaining reasonable transmission and optical correction in the 1230 nm range requires special objective lenses and other optical components (see Chapter 7, *this volume*).

How do the signals produced by these four lasers match the performance of the available detectors? Because the Ti:Sa wavelengths are well within in the sensitivity range of both high quantum efficiency (QE) silicon-based detectors and most PMT photocathodes, any scattered excitation illumination will be detected by these detectors and recorded as background. Although this reduces the signal-to-noise (S/N) ratio of fluorescence signals, it also affords the benefit of being able to detect the backscattered light (BSL) signal as an additional, non-damaging imaging modality.

On the other hand, because the emission wavelengths of Nd:glass and Cr:forsterite lasers are beyond the sensitivity of most of the commonly used PMT and silicon detectors (Table 40.2), detector insensitivity guarantees a low background level from scattered light but sacrifices availability of BSL modality unless a special NIR detector (e.g., InGaAs photodiode, Edmund Scientific) is installed. Table 40.2 lists the sensitivity, the sensitivity range, and the wavelength of maximum sensitivity for each of the photodetectors commonly used in microscopy (see also Chapter 12, *this volume*). Because the peak intensity of the ultra-fast laser is so high, a dichroic beam-splitter and a barrier filter may not be sufficient to exclude the background signal caused by light leakage. This is a particular problem when collecting SHG and THG signals in the transmission mode where the excitation striking the emission filter may be $10^7\times$ brighter than the SHG/THG signal. In this case, using detectors insensitive to the illumination wavelength can further limit the background signal level, improving the S/N of the image.

Using a Cr:forsterite or Nd:glass laser at 1230 nm/1064 nm for nonlinear microscopy allows one to fully utilize the transparent window in most biological specimens. At 1230 nm, Chu and colleagues found that the SHG and 2PF signal dropped by only 1 order of magnitude, when generated at a depth of 360 μm in a maize stem fixed in 70% ethanol (Chu *et al.*, 2001). This is in good agreement with previous light attenuation measurements of maize stems (Cheng *et al.*, 1998). Comparing the attenuation spectra of

TABLE 40.2. Characteristics of Photodetectors Used for SHG and THG Microscopy

Type	Photocathode Composition	Photoemission Threshold (nm)	Wavelength at Maximum Sensitivity (nm)	Radiant Sensitivity at λ_{max} (mA/W)	Quantum Efficiency at λ_{max} (%)
S1	AgOCs	1100	800	2.3	0.4
S4	$SbCs_3$	680	400	50	16
S11	$SbCs_3$	700	440	80	22
S13					
S20	$SbNa_2KCs$	850	420	70	20
S20 (extended-red multi-alkal)	$SbNa_2KCs$	900	550	35	8
Bialkali	SbKCs	630	400	90	28
Bialkali (green extended)	SbKCs	700	440	100	28
Solar blind	CsTe	340	235	20	10
		Spectral range		Photo sensitivity (A/W)	
Silicon photodiode		320 (190)–1100 nm	960 nm	0.33 (λ = 633 nm)	
InGaAs photo-diode		900–1700 nm	1550 nm	0.9 (λ = 1300 nm) 0.95 (λ = 1550 nm)	

The short wavelength limit of the PMT is determined by the window material (lime glass, 300 nm; borosilicate glass, 250 nm; fused silica, 180 nm. The short wavelength sensitivity cut-off of photodiode is also limited by the package window material; number in parentheses represents fused silica window. (Data adopted from Photonics, Brive, France and Hamamatsu Inc., Japan. QE data refer to the photocathode response only.)

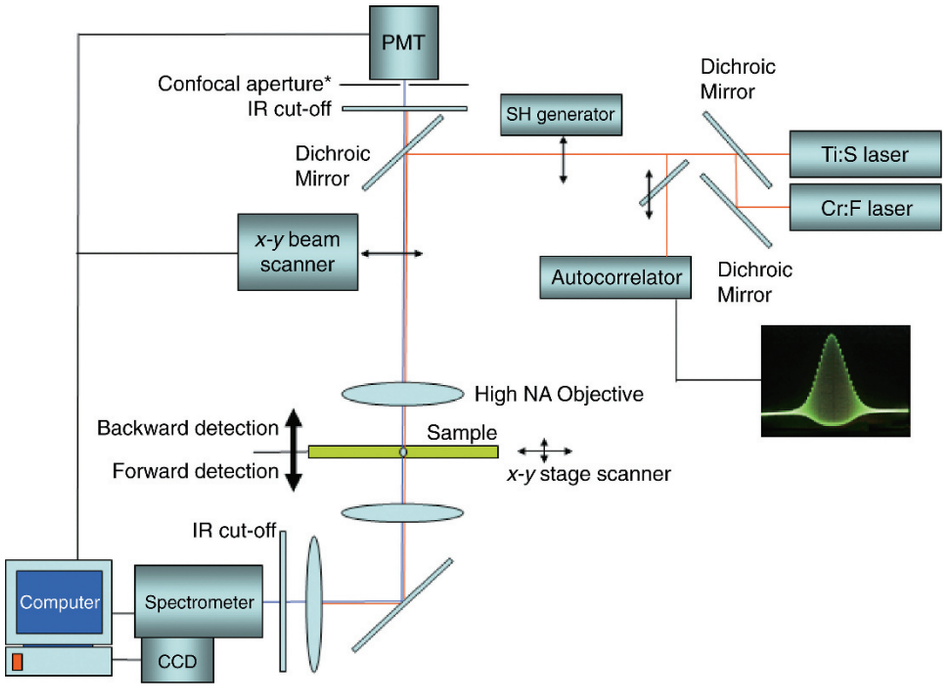

FIGURE 40.3. (A) Diagrammatic representation of a nonlinear laser-scanning microscope. The *xy*-beam scanner can be removed (by parking the *xy*-mirror at the center position) from the system to allow stage-scanning operation. An autocorrelator can be introduced into the beam to monitor the pulse width. A second harmonic generating crystal can also be introduced into the beam to allow the illumination to operate at λ/2. The spectrometer can also be connected to the epi-illumination path to detect the backward SHG signal. CCD, charge-coupled device; *, optional.

plant tissue with that of a chicken skin (Fig. 40.1), over the emission range of the Ti:Sa laser, one can expect significantly better depth penetration performance from Cr:forsterite/Nd:glass/ytterbium laser sources in brain-slice research. This superior depth performance agrees well with previous studies comparing the penetration depth of optical coherence tomography (OCT) between 800 nm and 1300 nm light (see Chapter 34, *this volume*; Bouma *et al.*, 1996).

Moreover, a significant reduction in photo-induced damage was observed in plant materials when 2PF microscopy was conducted using a femtosecond Cr:forsterite laser rather than a femtosecond Ti:Sa laser, under similar illumination intensity and exposure conditions (Chen *et al.*, 2002).

NONLINEAR OPTICAL MICROSCOPY SETUP

Figure 40.3 shows a diagrammatic representation of a typical imaging system for multi-modal, nonlinear microscope using either Cr:forsterite, Nd:glass, ytterbium, or Ti:Sa lasers (Cheng *et al.*, 2001b). In our setup, the laser beam profile is first shaped with a spatial filter and collimated by a beam expander to fill the back aperture of the objective lens. The collimated beam was coupled into an Olympus IX71 microscope through the confocal scanning unit with a 45° dichroic beam-splitter (Chroma 970dcspxr) to reflect the IR and transmit visible light. The original aluminum coating on the *xy*-scanning mirrors was replaced with a silver coating to enhance IR reflectivity. A second beam path was constructed to bypass the scan mirrors for fixed-beam, stage-scanning operation. The excitation IR light is focused onto the biological sample with a spot size close to diffraction limit using high-NA objectives [such as Olympus ULWD MIR 80×/0.75; or UPlanApo water-immersion 60×/1.20] and the excited photoemission spectrum was collected using an opposing high-NA objective (of the same type as the illuminating objective). The fundamental IR beam was removed with an infrared-blocking filter in conjunction with a dichroic beam-splitter (Chroma 970dcspxr). The collected light (visible and NIR) was then directed into a spectrometer (SpectraPro-2300i, Roper Scientific) and recorded by a Peltier-cooled charge-coupled device (CCD) detector (DV42-0E, Andor Technology). Transmission detection is used because most SHG and THG is emitted in the forward direction (i.e., in the same direction as the pump beam; Cheng and Lin, 1990).[1] In addition, a mechanical scanning stage is included to permit stable raster scanning so that *xyz*λ-images can be obtained. Is these images, a detailed nonlinear spectrum is recorded at each pixel (*xy*-plane is defined as the plane perpendicular to the laser propagation direction). The signal spectrum is obtained using a scanning spectrometer equipped with an InGaAs photodiode (Edmund Scientific). When beam scanning, a flat mirror is placed in the back-focal plane of the collector objective to send the SHG/THG signal back up the optical path so that it can be de-scanned and detected by the PMTs (the same setup as the transmission confocal microscope method discussed in Chapter 8, *this volume*). To obtain an image with a set signal wavelength, we used a simple scanning-monochrometer method, adopted from astronomy. The actual system is shown in Figure 40.4.

Although it is possible to select harmonic signals using narrow bandpass interference filters, it is important to take special precautions if the bandpass filter is used to isolate the SHG signal from multi-photon-excited fluorescence. In certain types of specimen, where the fluorescence emission wavelength generated by

[1] Recent results have shown that, in certain biological structures, backward SHG signals can be even stronger than forward SHG signals (Sun *et al.*, 2005).

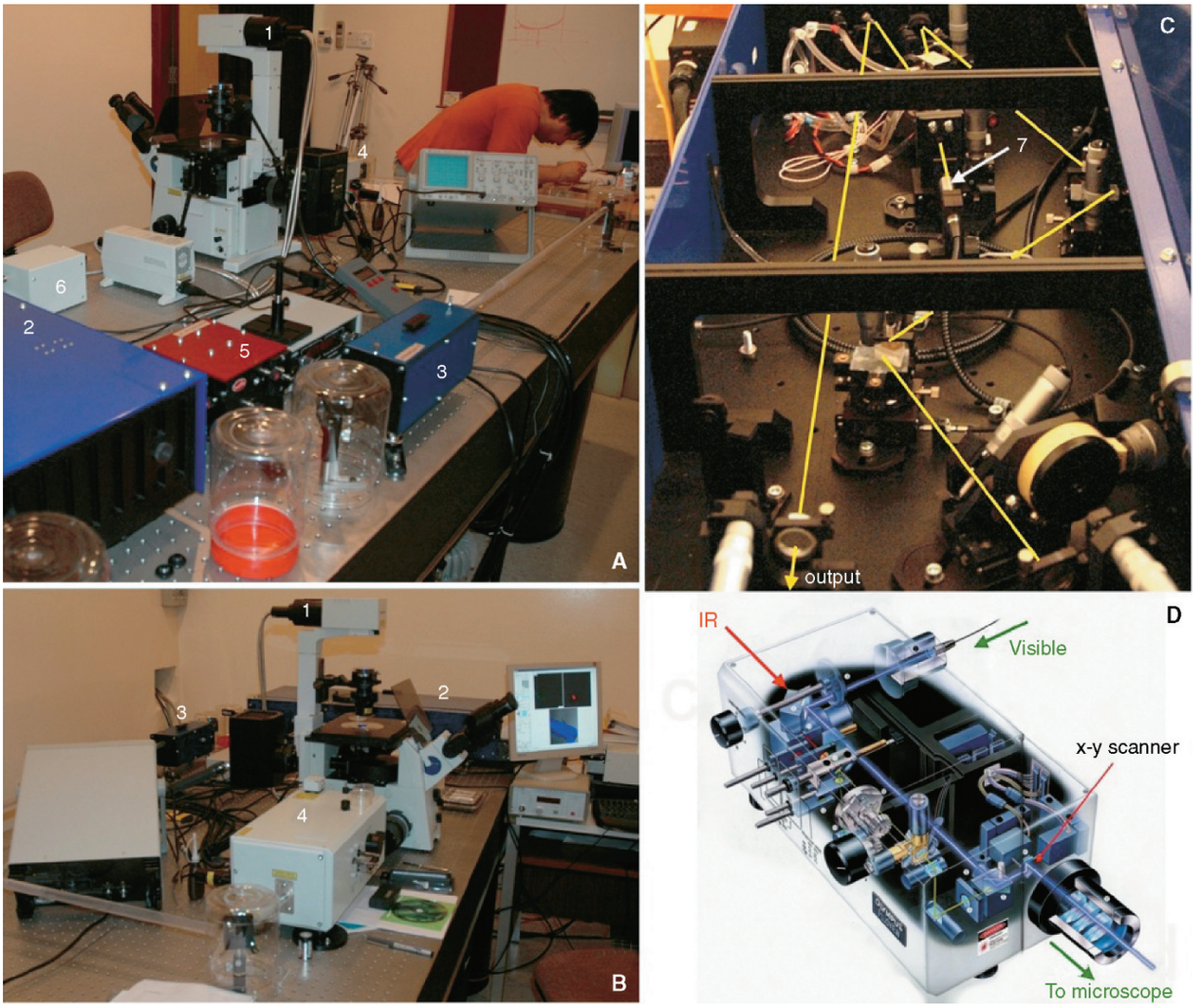

FIGURE 40.4. The nonlinear microscope setup in the laboratory of one of the authors (PCC) at the Department of Biological Sciences, National University of Singapore (A, B). The system is based on a mode-locked, ultra-fast Cr:forsterite laser (65 fs; 120 MHz; tuning range, 1230–1270 nm) (C) and an Olympus Fluroview FV300 confocal scanning unit (D). 1, transmission detector fiber connection; 2, Cr:forsterite laser; 3, SH generator; 4, beam scanner; 5, autocorrelator; 6, transmission detector; 7, pump input for Cr:forsterite laser.

three-photon excitation coincides with the SHG wavelength, spectral contamination can be serious even when a narrow-bandpass SHG isolating filter is used. Figure 40.5(A) shows a fluorescence spectrum when LysoTracker Red (Molecular Probes, Inc., L7528) is excited by Cr:forsterite laser at 1240 nm. If a biological specimen is stained with the dye and imaged simultaneously in SHG and fluorescence mode, the expected SHG signal is at 620 nm and THG at 413 nm, but the multi-photon-excited fluorescence (both 2PF and 3PF) of LysoTracker Red extends from ~580 nm to 720 nm. Therefore, even a very narrow bandpass filter centered at 620 nm will allow significant fluorescence contamination in the SHG signals, particularly if the SHG is relatively weak.

The best way to obtain a "pure" SHG signal is to use a monochrometer. Figure 40.5(B) shows the emission spectrum of the red leaf of *Euphorbia pulcherrima* (poinsettia) excited by 1234 nm IR, and the fluorescence emission consisting of 2PF and 3PF. Note the position of the SHG at 617 nm. No trace of SHG can be recognized in this spectrum because, in this case, the SHG is in the forward direction with respect to the illumination beam, while this spectrum was recorded from the same side as the incident illumination.

Figure 40.5(C) shows the emission spectrum of the leaf of *Zea mays* (corn). The fluorescence emission is in the red region and a small peak at 617 nm is the SHG signal scattered back from the leaf tissue. Because the SHG signal propagates in the same direction as the illumination beam, placing detector on the far side of the specimen will ensure better signal strength. Figure 40.6 shows nonlinear absorption by a methanol extract from the yellow petals of *Canna*. Readers are also referred to the nonlinear absorption spectrum of the highly efficient APSS fluorophore [(Fig. 8.5(A)]. Sun and colleagues (2003) have reported that using a longer

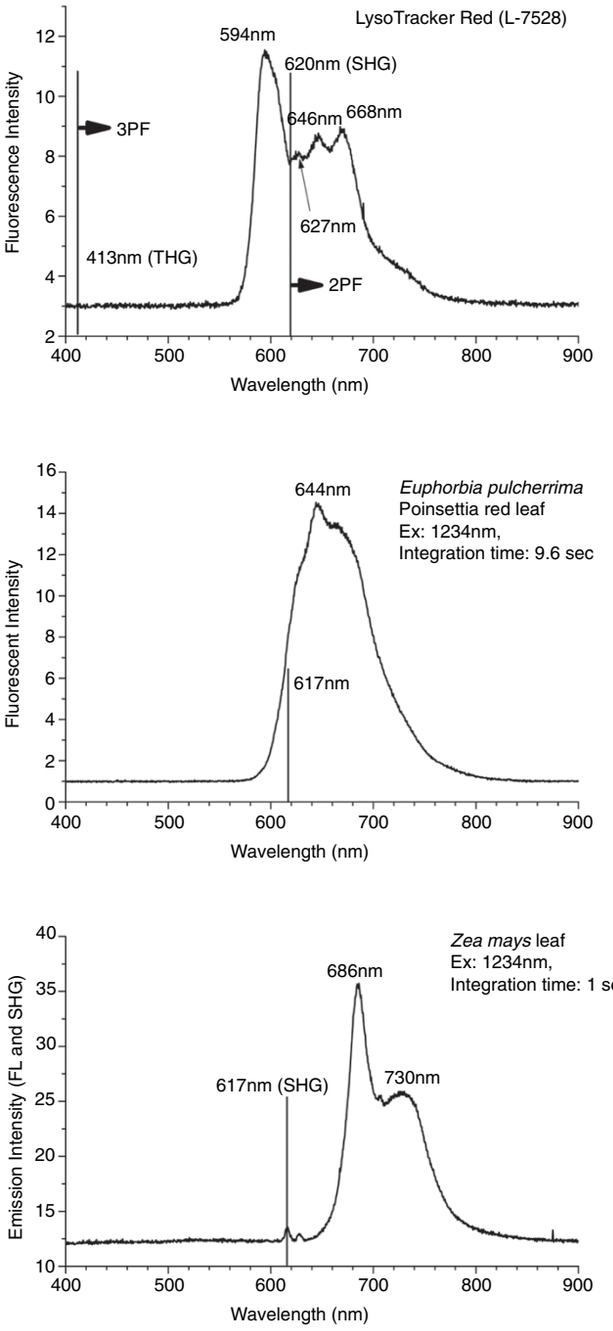

FIGURE 40.5. Two-photon fluorescence spectra of three different samples. (Top) LysoTracker Red (L-752, Molecular Probes), excitation at 1240 nm; (middle) red leaf of *Euphorbia pulcherrima* (excitation, 1234 nm); and (Bottom) leaf of *Zea mays* (excitation, 1234 nm), note the small SHG peak at 617 nm. The top two spectra show overlap between the 2PF emission and that from SHG.

wavelength excitation (1230 nm vs. 800 nm) can minimize the two-photon autofluorescence signal, hence improve the S/N in harmonic generation images. However, it is not clear if this reduction in autofluorescence intensity corresponds to a lower nonlinear absorbance of the specimen or a reduction in the quantum yield of the fluorophore.

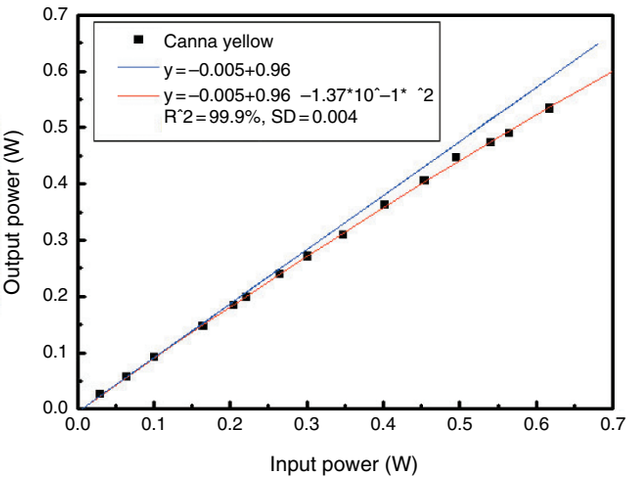

FIGURE 40.6. Nonlinear absorption of the methanol extract of the yellow petal of *Canna*. (Measurement was performed by Ms. Mei-Hsin Chen, Graduate Institute of Electro-Optical Engineering and Department of Electrical Engineering, National Taiwan University, Taipei, Taiwan.)

OPTICALLY ACTIVE BIOLOGICAL STRUCTURES

Optically Active Structures in Plants

The cell wall of higher plants consists of macrofibrils, which are orderly bundles of cellulose microfibrils each with a diameter about 10 nm. Within the microfibrils are micelles, representing another degree of highly ordered crystalline structure (Peter *et al.*, 1992). These photonic-crystal–like structures produce the optical anisotropy that gives rise to SHG. Figure 40.7(A) shows the nonlinear emission spectra measured from the cell wall of a parenchyma cell in maize stem (*Zea mays* L.). Symmetric THG and SHG emission peaks are visible, centered at 410 nm and 615 nm, with an intensity similar to or stronger than the two-photon autofluorescence centered at 680 nm. The strong THG signal is induced by the optical inhomogeneity within, and surrounding, the cell wall, while the SHG signal reflects the highly organized crystalline structures in the wall that break three-dimensional (3D) optical centro-symmetry. Figure 40.7(B–D) shows the THG, SHG, and 2PF images made by detecting wavelengths corresponding to the peaks in the spectrum shown in Figure 40.7(A). The source of SHG is further confirmed by the strong SHG signal obtained from the stone cell of pear (*Pyrus serotina* R.) (Fig. 40.8). The extensive secondary wall development of the sclerenchyma cell generates significant SHG signals.

The starch granule, a highly birefringent structure, consists of crystalline amylopectin lamellae organized into effectively spherical blocklets and large concentric growth rings (Gallant *et al.*, 1997) (Fig. 40.9). The crystalline lamellae in starch granules are believed to consist of the ordered, double-helical amylopectin side chains and are interleaved with more amorphous lamellae consisting of the amylopectin branching regions. The amylopectin side-chain clusters within the crystalline lamellae have varying sizes but, on average, are around 10 nm wide by 9 to 10 nm long (the length represents the thickness of the lamellae). These orderly nanolayers form the biophotonic structure, breaking the centro-symmetry and producing strong SHG. On the other hand, starch granules contain other, larger structures made up of crystalline hard shells and semi-crystalline soft shells having dimensions of hundreds of nanometers. These alternating crystalline and semi-

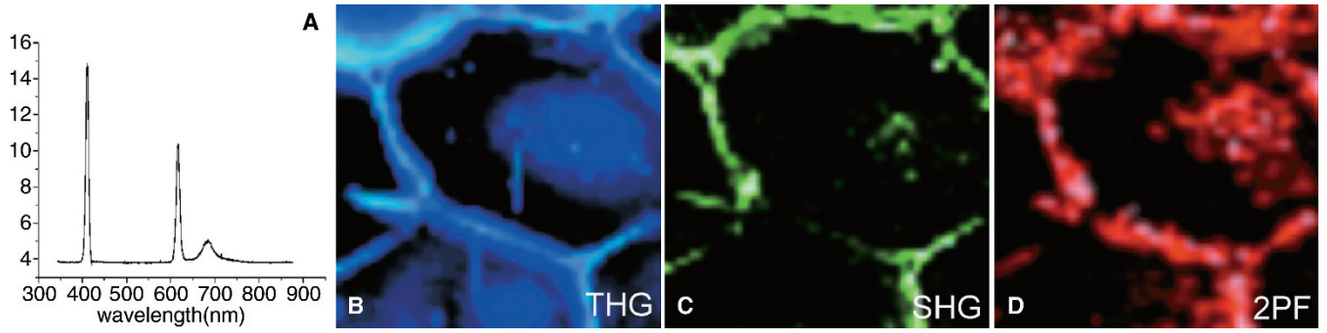

FIGURE 40.7. Nonlinear emission spectra measured from the cell wall of a parenchyma cell in maize stem (*Zea mays*). (A) The spectrum present a point in the image of (B); (B) THG image; (C) SHG; and (D) 2PF images.

crystalline rings have spatially-modulated nonlinear properties that could behave as 3D nonlinear photonic bandgap crystals (Berger, 1998) and may be responsible for the strong SHG observed. For example, the SHG signal from a potato (*Solanum tuberosum* L.) starch granule is so strong that is visible to the naked eye, even under ambient room light (Fig. 40.10). This unexpectedly strong SHG activity may be the result not only of the superhelical amylopectin nanostructure but also suggests that the specimen may be acting as a collection of 3D photonic bandgap crystals, the reciprocal lattice basis vectors of which would be capable of producing SHG by meeting the non-collinear phase-matching condition. Depending on the illumination wavelength and the materials of which the specimen is composed, the spatial frequencies present in high-order structures from 200 nm to 10 μm in size, can provide the non-collinear phase-matching base vector needed to produce SHG. The potato specimen is acting as an array of nonlinear, biophotonic bandgap crystals.

Figure 40.11(A–C) shows THG, SHG, and 2PF images, respectively. of a mesophyll cell of *Commelina communis* L.; Figure 40.11(D) is the corresponding three-channel, false-color image. The THG image shows the interface signal between the chloroplast and the surrounding cytoplasm while the SHG reveals starch granules and possibly grana and thylakoid membranes in the chloroplasts and the 2PF results from chlorophyll autofluorescence. Enlarged images of individual chloroplasts are shown in Figure 40.11(E–H).

The distribution of chlorophyll inside the chloroplasts is shown by the 2PF signals while THG signal provides information on various sub-organelle interfaces. SHG signal, on the other hand, indicates the presence of nano-organized biophotonic structures in the chloroplast. By matching the SHG image with transmission electron microscope (TEM) images of similar specimens, it has been possible to conclude that the SHG signals are produced by stacked thylakoid membranes present in the grana (crescent shaped) and by highly birefringent starch granules (oval or round shaped) in the chloroplasts (Gunning and Steer, 1996). The stacked thylakoid membranes of the grana and the orderly deposits of amylopectin in the starch granules provide the structural requirement for efficient SHG, again resembling the behavior of photonic crystals.

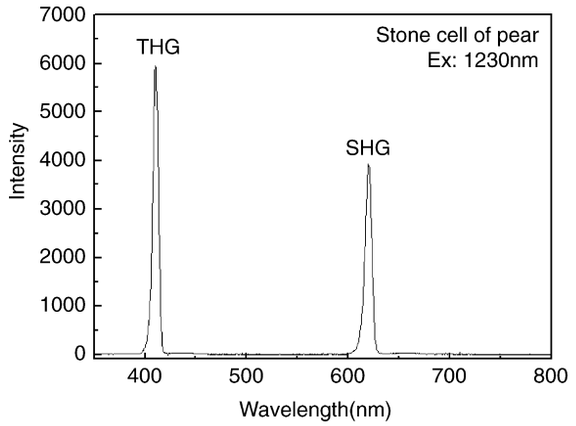

FIGURE 40.8. Spectrum of the stone cell of a pear fruit (*Pyrus serotina* R.) recorded with 0.1-s integration time.

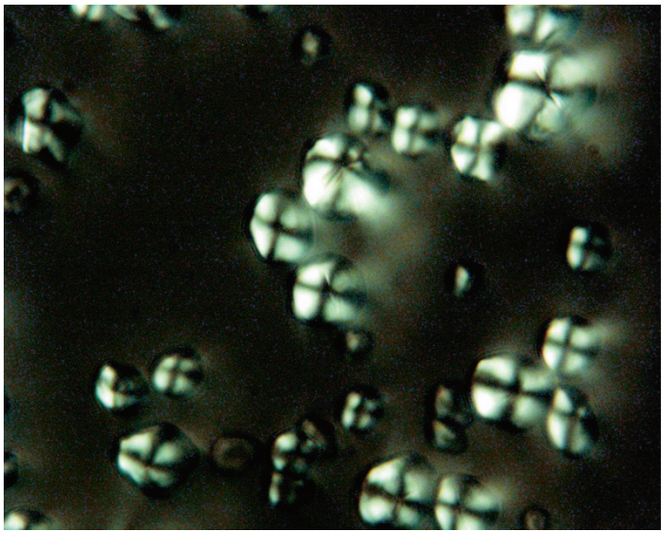

FIGURE 40.9. Conventional polarization microscopy of maize starch granules. The image was taken with an oblique-illuminated microscope equipped with cross-polarizer. Note the strong birefringence of the starch granules.

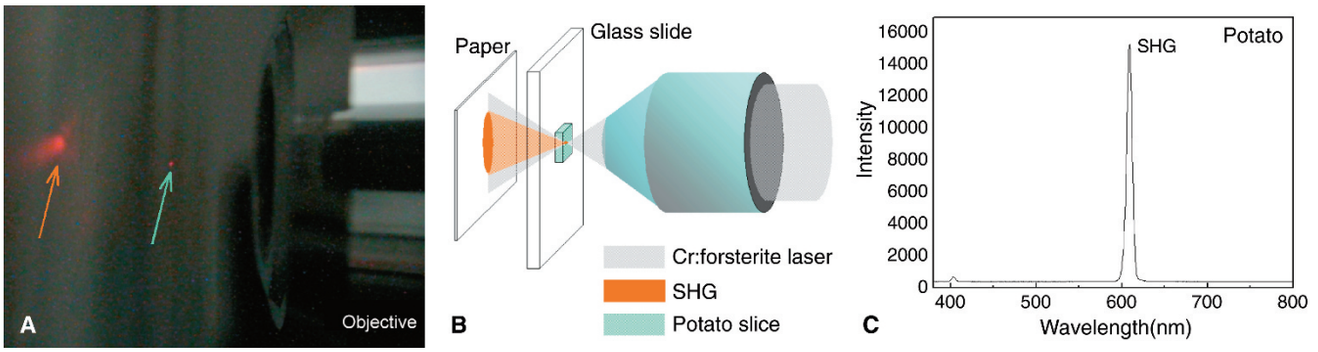

FIGURE 40.10. Photograph showing the red SHG signal generated from a thin slice of potato tuber (*blue arrow*) by a focused laser beam at a wavelength of 1230 nm and projected onto a white paper (*orange arrow*) (A). As this photograph was taken with a conventional camera, which is insensitive to 1230 nm light, the small red spot on the potato slice is the scattered SHG signal. The corresponding setup is schematically shown in (B). The emission spectrum is shown in (C).

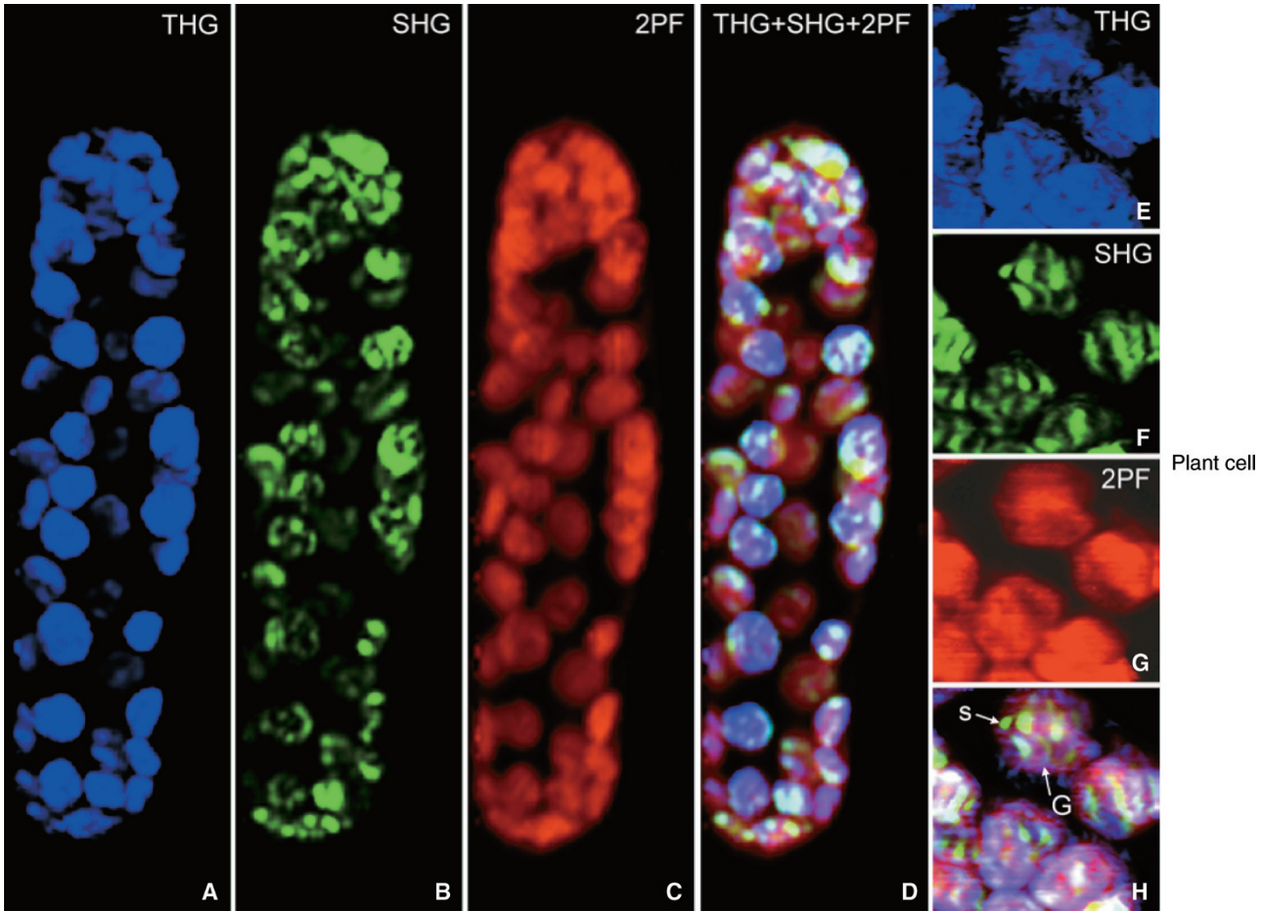

FIGURE 40.11. Harmonic and fluorescence images of a mesophyll cell of *Commelina communis* L. (A) THG image; (B) SHG image; (C) 2PF image; (D) false-color image of the combination of THG-SHG and 2PF. (E–H) High magnification images of chloroplasts showing strong SHG generation from starch granules (s) and possible grana (G). Ex, 1230 nm.

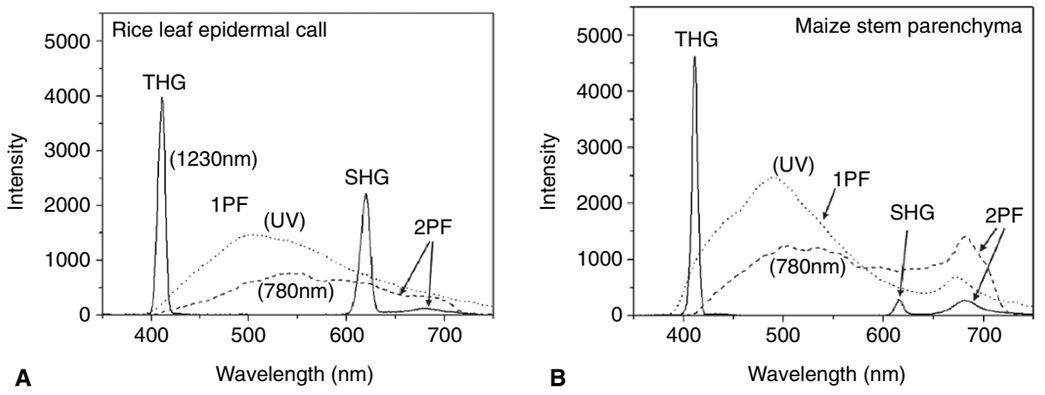

FIGURE 40.12. Nonlinear emission spectra from the cell wall of (A) an epidermal cell in rice leaf and (B) parenchyma cells in maize stem with three different sources: UV light (dotted *line*), 780 nm pulsed signal (*dashed line*), and 1230 nm pulsed laser (*solid line*). The suppression of background 2PF and the symmetric peaks of THG and SHG in 1230 nm excitata spectra are evident.

The tumbling movement of chloroplasts in cytoplasm results in changes in the apparent periodicity of the thylakoid membrane stacks along the direction of the illuminating beam. This tumbling therefore changes the SHG efficiency, a fact that can be used to study chloroplast tumbling, a phenomenon that is difficult to study by other means.

Compared with the emission spectra excited by a femtosecond Ti:Sa laser in these plant specimens, the intrinsic 2PF signals are generally reduced by using a longer wavelength as the pumping source (Chu *et al.*, 2001). As an example, Figure 40.12 shows a quantitative comparison between the emission spectra excited by a 150 mW 1230 nm Cr:forsterite femtosecond laser (120 fs pulse width, solid line), a 50 mW 780 nm Ti:Sa femtosecond laser (120 fs pulse width, dashed line), and a 0.45 mW 365 nm UV light source from a frequency-doubled Ti:Sa laser (dotted line). The emission spectra from the cell wall of rice leaf (*Oryza sativa*) epidermis and of the parenchyma cells in a maize stem are shown in Figure 40.12(A,B), respectively. Broad autofluorescence covering the whole visible and NIR region is evident with both UV (single-photon fluorescence) and 780 nm excitation (2PF); whereas with 1230 nm excitation, only weak residual 2PF and efficient harmonic generation were observed. With background autofluorescence suppressed by using a longer excitation wavelength, the whole visible and NIR region is available for detecting signals from specially designed, multi-photon excited fluorescence dyes that can be used to label different functional molecules (Cheng *et al.*, 1998). Furthermore, as there is no energy deposition at all during harmonic generation processes, no photodamage effect is expected with SHG and THG. Thus, with efficient SHG and THG signals, along with the reduced but still-measurable intrinsic 2PF signals, the longer wavelength light source appears to be a better choice for intrinsic harmonic generation imaging because it leaves a wider spectrum available for extrinsic multi-photon dye labeling. Figure 40.13 compares the emission spectra of maize leaf and stem (epidermal cells) when excited by 1230 nm, 780 nm, and 400 nm.

Figure 40.14 shows the specific *xy*λ-images corresponding to THG, SHG, and 2PF in the parenchyma cells of a maize stem, taken at a depth of 110 µm from the sample surface. The total sample thickness was around 500 µm. With an average power of 100 mW before entering the sample and a focused spot diameter of ~1.3 µm, the intensity at focus ranges from 9 to 50×10^{10} W/cm,[2] depending on the focal depth inside the sample. As expected, strong SHG and THG can be observed in the cell wall. THG shows the longitudinal cell walls in the center of the image as well as the transverse cell walls of several adjacent cells [Fig. 40.14(A)], This demonstrates the ability of THG to pick up the outline of the whole cell. SHG may show the relative position of the secondary walls (arrows). In regions with extensive secondary wall growth, the separation of the secondary wall can be clearly observed in Figure 40.14(B) and the 2PF signal indicates the distribution of fluorescent molecules [Fig. 40.14(C)]. By comparing different images made using different modalities, one can image the relation-

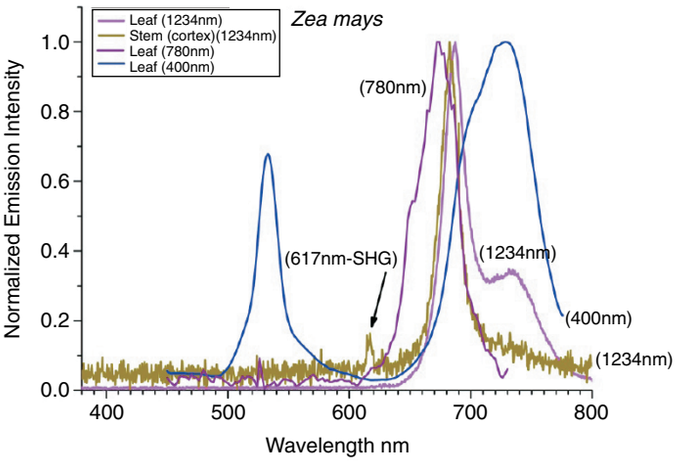

FIGURE 40.13. Normalized emission spectra of maize tissue under different types of excitation. 1PF at 400 nm (blue). Two-photon excited spectra generated at 1234 nm from a leaf (green) lacks the hump due to fluorescence of the cell wall found in stems (magenta). It also lacks the SHG peak at 617 nm, probably generated by the secondary cell walls in the stem sample. Two-photon excitation at 780 nm produces fluorescence (maroon) that peaks at a shorter wavelength than the fluorescence excited by the other modes.

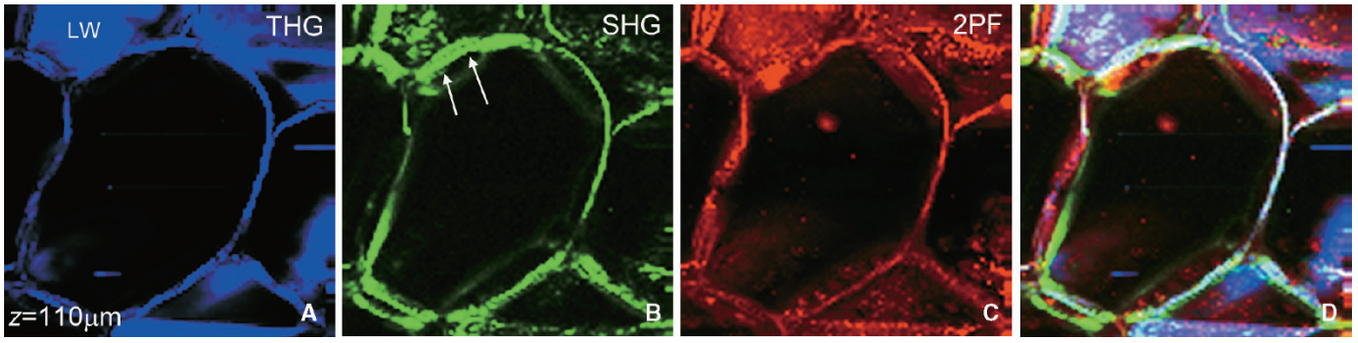

FIGURE 40.14. Optical section obtained near the longitudinal wall (LW) of a parenchyma cell in maize stem. Note the strong THG from the radial wall (RW) (A), the SHG (B), 2PF (C), and combination of THG-SHG-2PF (D). *Arrows*: possible secondary wall material. The image was obtained 110 μm below the surface of the specimen.

ships between structural (harmonic generations) and chemical information (two- and multi-photon fluorescence) in biological tissues. A penetration depth of more than 500 μm has been achieved in the maize stem sample with 1230 nm excitation (Chu *et al.*, 2001).

Figure 40.15 shows paradermal optical sections of the adaxial surface of rice (*Oryza sativa* L.) leaf. THG provides structural interfaces, such as the papillae from the cuticular layer and the cell wall of bulliform cells [Fig. 40.15(B)]. As expected, SHG reflects biophotonic structures including the cuticular papillae and longitudinal cell walls [Fig. 40.15(B)], due to the orderly arrangement of cutin, waxes, and cellulose microfibrils, respectively. 2PF, on the other hand, picks up the fluorescent chromophores [Fig. 40.15(C)]. Figure 40.16 shows a through-focus series (5 μm step) of an area on the surface of rice leaf where silica cells can be found (Hodson and Sangster, 1989; Cheng 1987, Cheng *et al.*, 1990). Note the outline of the silica cell in the THG images and the high SHG signals from the silica deposits. A strong SHG signal can also be obtained from the silica wall of a diatom.

Optically Active Structures in Animal Tissues

There are many structures in animal tissue that are also good candidates to produce a strong biophotonic effect (Table 40.3). For example, the sarcomeres in skeletal muscles are composed of crystalline myosin and actin nanofilaments, with periods of 40 and 20 nm, respectively, that fall into the spatial range required for strong SHG activity. Figure 40.17 shows longitudinally sectioned *xy*-images obtained from the somites of a zebrafish embryo. The cardiac muscle fiber produces intense SHG signal [green, Fig.40.17(A–D)] and the surfaces of the red blood cells (RBC) produce intense THG signal [blue, Fig. 40.17(C,D)].

Figure 40.18 shows a two-channel harmonic image of somites in a zebrafish embryo. At low magnification, the somites are seen to be separated by clefts [Cl, Fig. 40.18(A)]. At higher magnification [Fig. 40.18(B,C)], the green SHG image of the sarcomeres (s: between the two arrows) indicate that the strong blue THG signal in Figure 40.18(A) is probably generated by the optical discontinuity occurring between the somites. The SHG intensity difference in individual sarcomeres [Fig 40.18(C), between arrows] reflects differences in the spatial packing of F-actin and myosin in dark bands and light bands. The strong SHG activity from the actin/myosin complex can make harmonic imaging a useful tool for the study of muscle cell dynamics as the arrangement changes during muscle contraction and relaxation.

Microtubule bundles are birefringent structures that can be studied in living cells using polarization microscopy. Recent

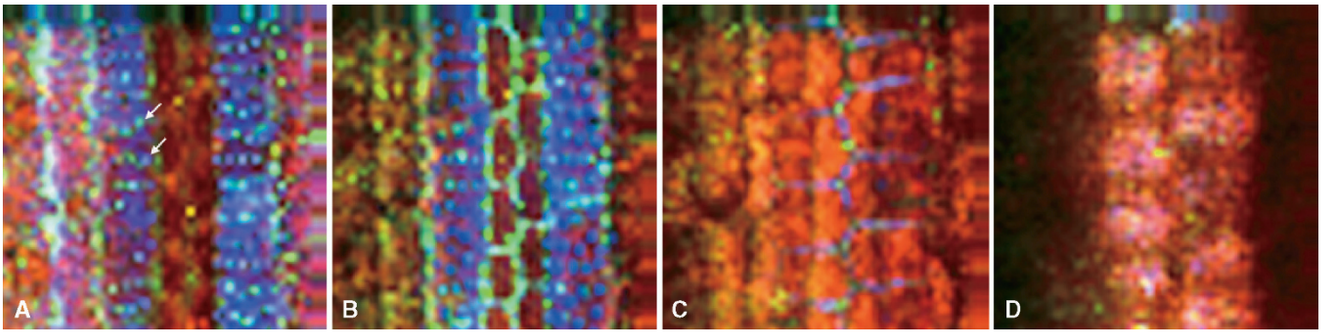

FIGURE 40.15. Through-focus, three-channel harmonic fluorescence images of the adaxial surface of rice leaf. (A) Near surface, (B) epidermal cells, (C) epidermal–mesophyll interface, (D) mesophyll cells. Note the strong 2PF emission from the chlorophyll of the mesophyll cells. *White arrows*: cuticular papillae.

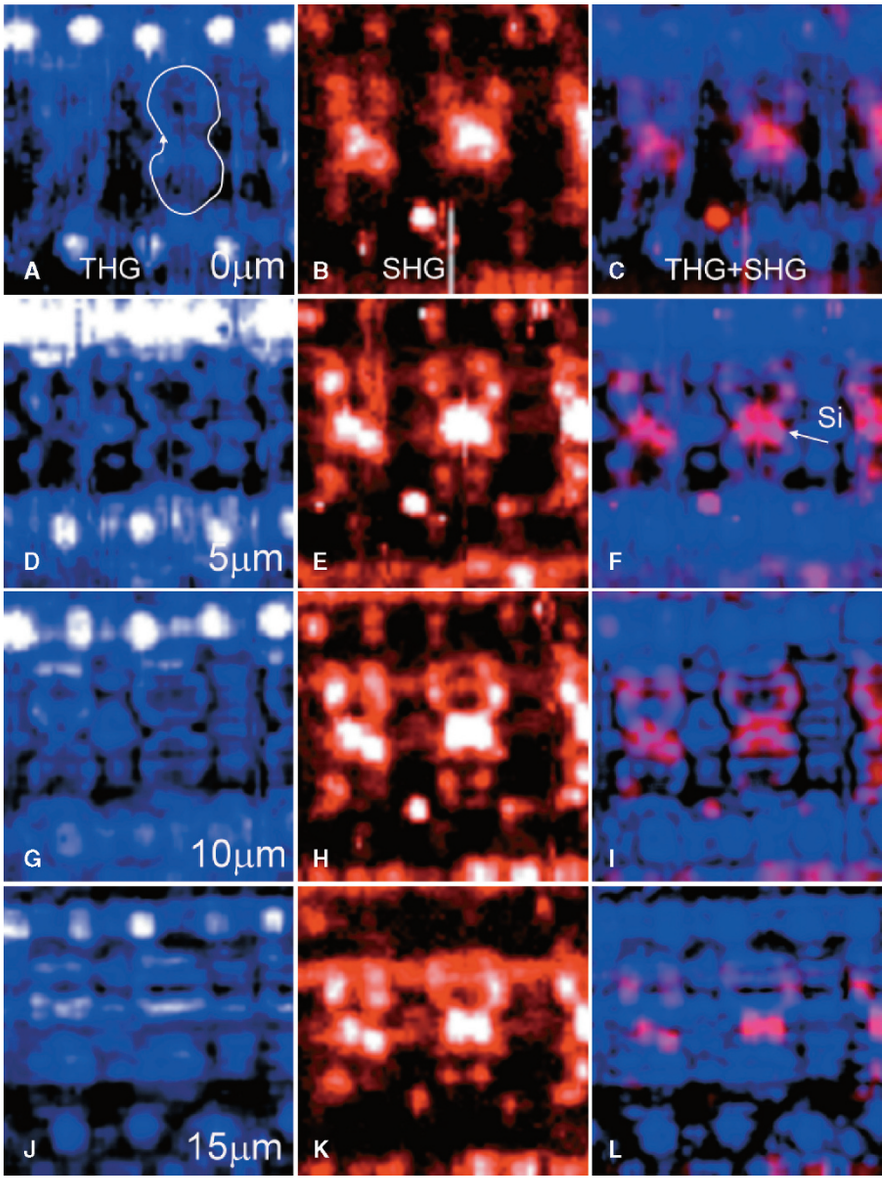

FIGURE 40.16. Through-focus, two-channel images of the surface of rice leaf, showing a silica cell. As it can be seen in the focal series (A–D), the SHG signal is generated by the bulk of the phytolith (Si), not by the surface of the silica deposit.

advances in dynamic polarization microscopy utilizing tunable liquid–crystal polarizers now allow one to study cytoskeleton dynamics and spindle behavior. The technique not only provides information on the retardance of the birefringent structure, but can also provide data of the molecular orientation of the structures (*s*-axis) (Oldenbourg and Mei, 1995).

Figure 40.19 shows a typical example in which polarization microscopy has been used to determine the orientation of the collagen fiber scaffold in an engineered tissue. Polarization microscopy can also allow one to directly visualize the spindle during cell division under low light conditions. Figure 40.20 shows the spindle of a fertilized oocyte during a cloning operation. Microtubules have also been shown to produce strong SHG signal in both the forward and the backward configurations (Sun *et al.*, 2005). Figure 40.21 demonstrates the specificity of the SHG signal from the spindle apparatus of a developing zebrafish embryo. The interface between the cell membrane and the surrounding aqueous medium produces a strong THG signal (blue) that provides the

TABLE 40.3. Biological Structures that Produce Harmonic Signals

Structures	Birefringence	SHG
Microtubules	+	+
Microfilaments	+	+
Spindle	+	+
Collagen fiber	+	+
Elastic fiber	+	+
Cuticle	+	?
Cuticular wax	+	?
Sarcomere	+	+
Grana and thylakoid	?	+
SiO2 deposit	+	+
Starch granules	+	+
Cell wall	+	+
Bone matrix	+	+
Dentine	+	+
Enamel	+	+

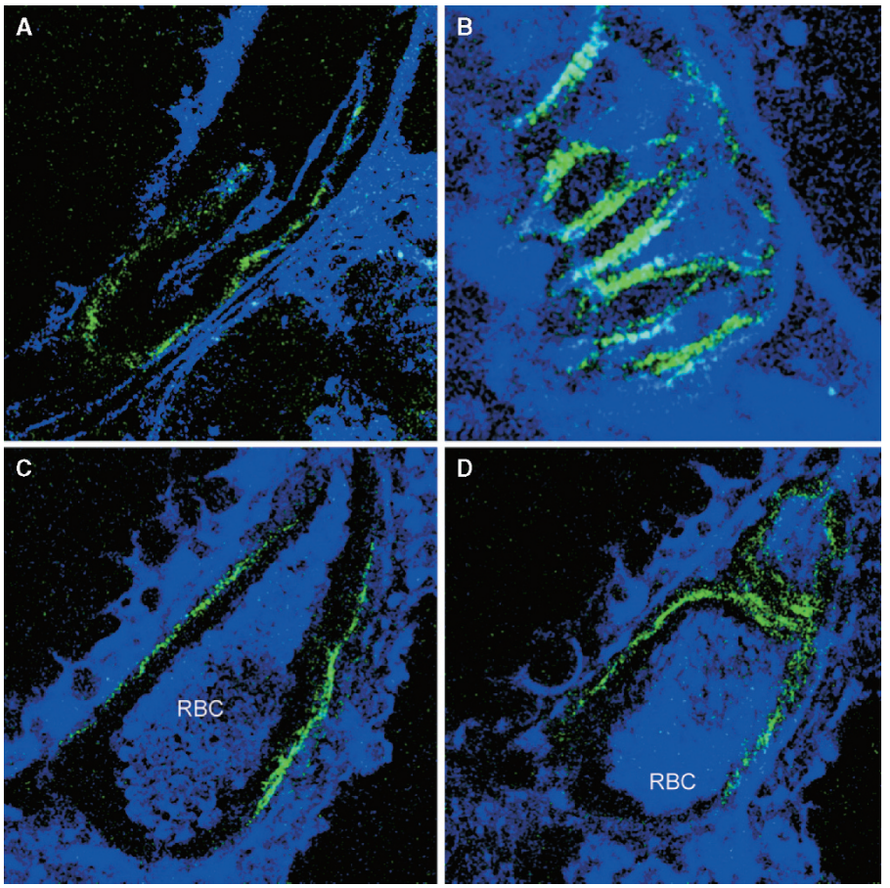

FIGURE 40.17. Two-channel, harmonic images of developing heart in a zebrafish embryo. The cardiac muscle fiber produces intense SHG signal (green, A–D). The red blood cells (RBC) produce intense THG signal (blue, C and D).

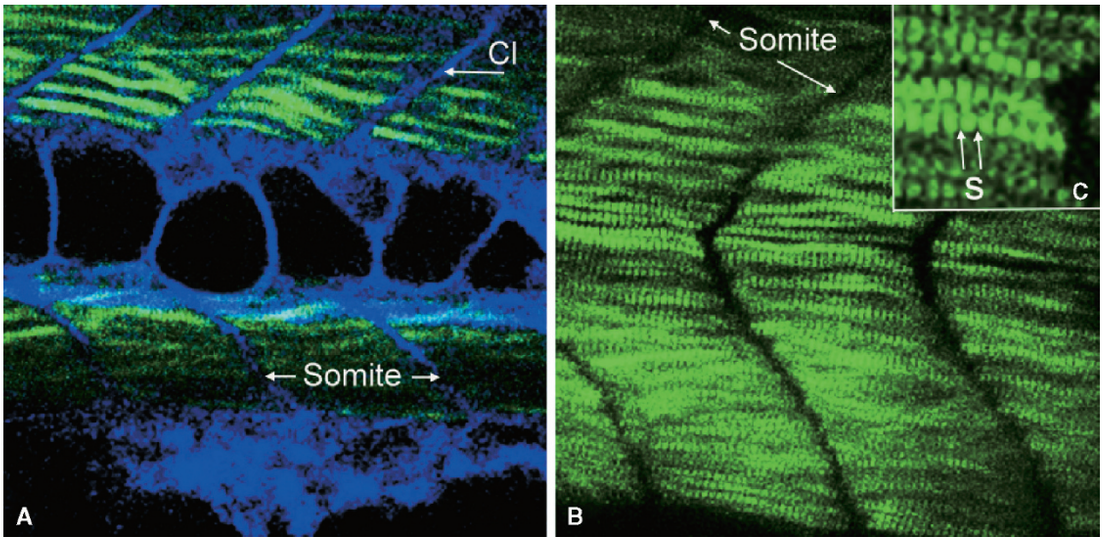

FIGURE 40.18. Two-channel harmonic image of somites in a zebrafish embryo. (A) Low magnification view of the somites separated by clefts (Cl); SHG, green; THG, blue. (B) SHG image showing developing myofibrils. Note: individual sarcomeres are clearly visible. (C) Higher magnification, SHG image of the sarcomere (s: between the two arrows) indicating that the strong SHG signal is likely generated from the dark band of sarcomere.

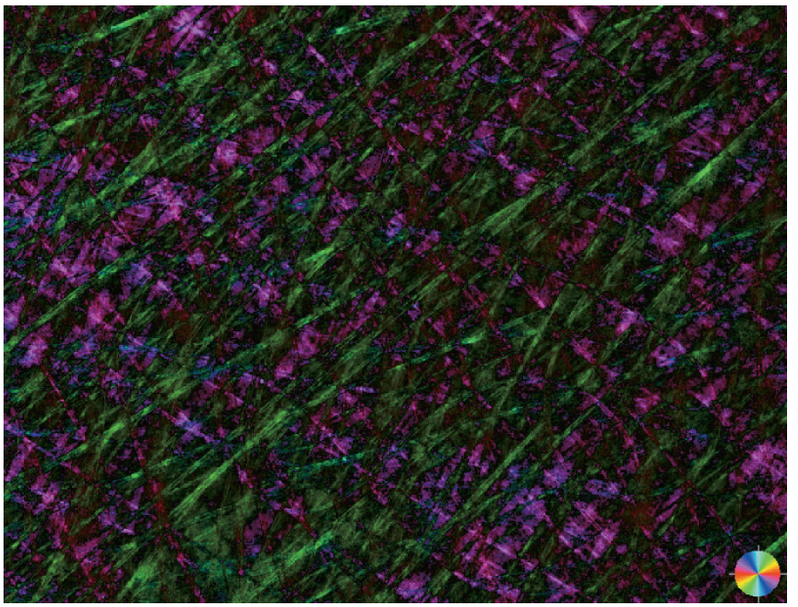

FIGURE 40.19. Polarization microscopy of man-made collagen fiber. The image demonstrates the orientation of the collagen fiber imaged by using a Polscope. The color wheel indicates the orientation of the *s*-axis of the collagen fiber. (Image courtesy of Prof. Hanry Yu, Department of Physiology, National University of Singapore.)

general outline of the embryo. Figure 40.20 is a set of high magnification, polarization microscope images showing a cell in various stages of cell division.

As multi-harmonic imaging (SHG and THG) allows deep-tissue imaging of biological specimens, it is suitable in developmental biology where larger specimens are commonly encountered. The use of a high-repetition-rate Ti:Sa laser offers the possibility of real-time, harmonic imaging of biological specimens (Chu *et al.*, 2003a; Sun *et al.*, 2002).

Collagen fibers are abundant in animal tissue, and are both birefringent and capable of producing SHG signals. SHG is now often used to visualize the orientation-dependent properties of connective tissue and the extracellular matrix (Roth and Freund, 1979, 1981; Freund *et al.*, 1986; Guo *et al.*, 1997; Stoller *et al.*, 2002a,b; Zipfel *et al.*, 2003; Williams *et al.*, 2005).

Polarization Dependence of Second Harmonic Generation

SHG signal strength from biophotonic structures varies according to the relative orientation between the beam and the organized structure. This allows one to study the orientation of a structure using SHG with controlled illumination polarization. For example, the dumbbell-shaped silica deposits on rice and maize leaves produce intense SHG signals. By varying the incident light polarization (Fig. 40.23), the concentrically deposited silica layers in the lumen of silica cells (Hodson and Sangster, 1989) produces SHG images that depend on the orientation of the illumination polarization. The polarization direction of the excitation is marked in the LR corner of the left-hand image in each row. The white outlines in Figure 40.23(A) demarcate the locations of two dumbbell-shaped silica cells. In contrast, no polarization dependency is evident in THG images. It is possible to isolate the epidermal cuticle with the attached phytolith (silica deposits) by $ZnCl_2$—HCl treatment. The fact that images of these isolated, silica deposits reveal little polarization dependency in the SHG signal (Fig. 40.24) suggests that the organic matrix on which the silica is deposited is the source of the photonic activity in the phytolith. Polarization-dependent contrast can also be used to study the orientation of collagen fibers in tissue engineering research (Freund *et al.*, 1986; Stroller *et al.*, 2002a,b; Chu *et al.*, 2004).

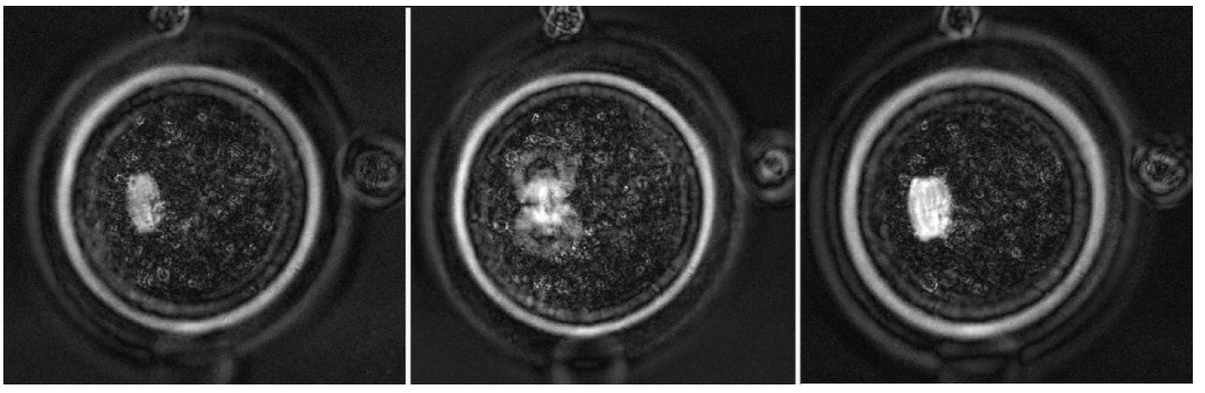

FIGURE 40.20. The spindle apparatus in the first division of a mouse zygote imaged by polarization microscopy. [The image was obtained by Ms. Gina Chen of Ming-mei Technology, Taipei, using a Spindleview dynamic polarization microscope (Cambridge Research Instrument, Cambridge, MA).]

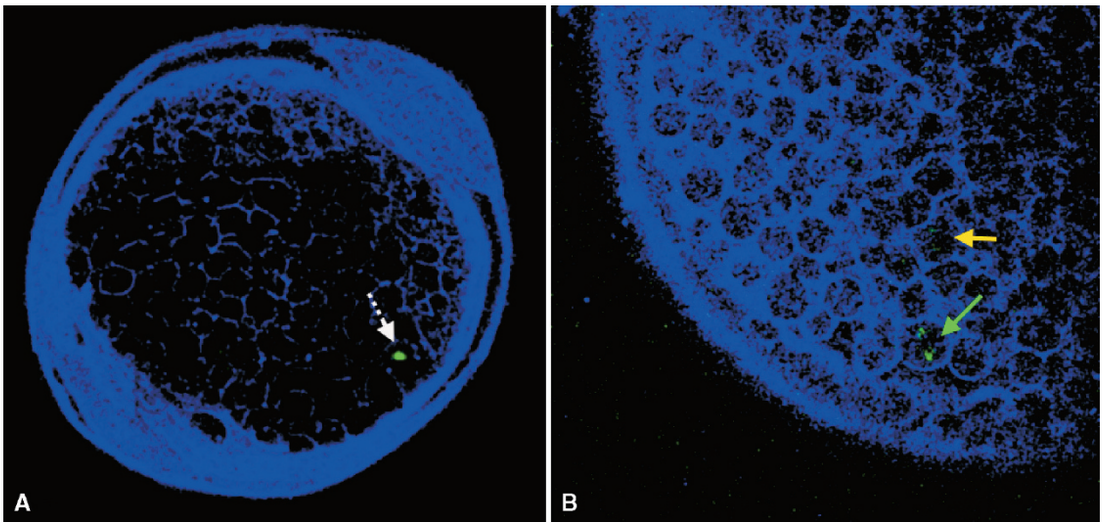

FIGURE 40.21. Dual-channel, harmonic image of a zebrafish embryo showing the cells and the embryo outlined by THG (blue) and a mitotic spindle (green, *arrows*) in SHG. (A) Overall view of the embryo; (B) part of the embryo showing cells in telophase (*yellow arrow*) and anaphase (*green arrow*).

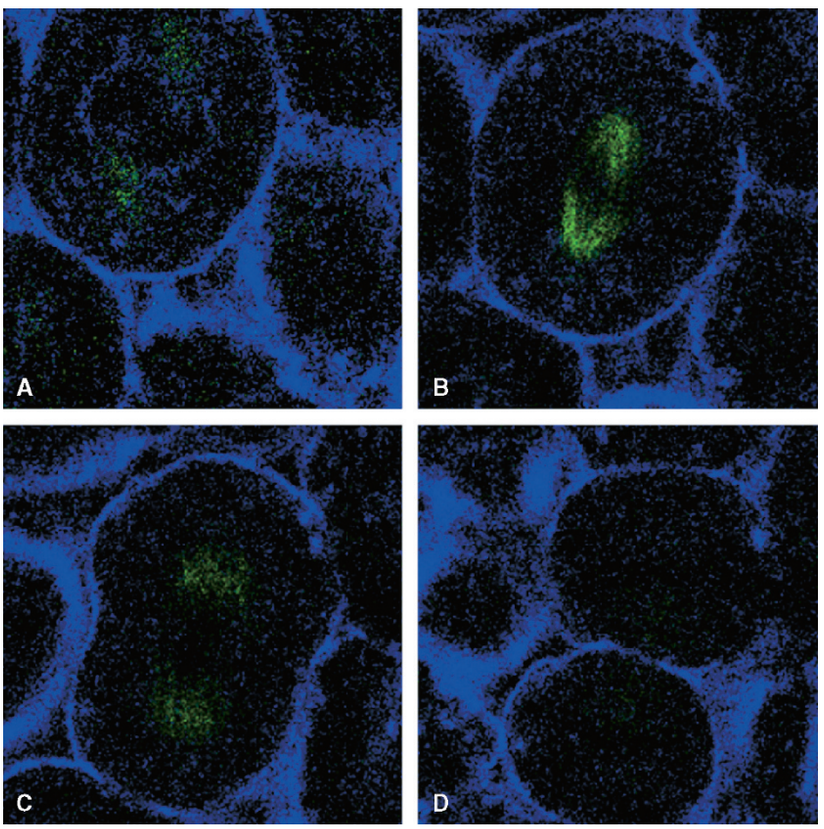

FIGURE 40.22. High magnification views of various stages in the formation of the spindle in a zebrafish embryo. (A) Telophase, (B) anaphase, (C) late anaphase, and (D) after cytokinesis, viewed in SHG (green) and THG (blue).

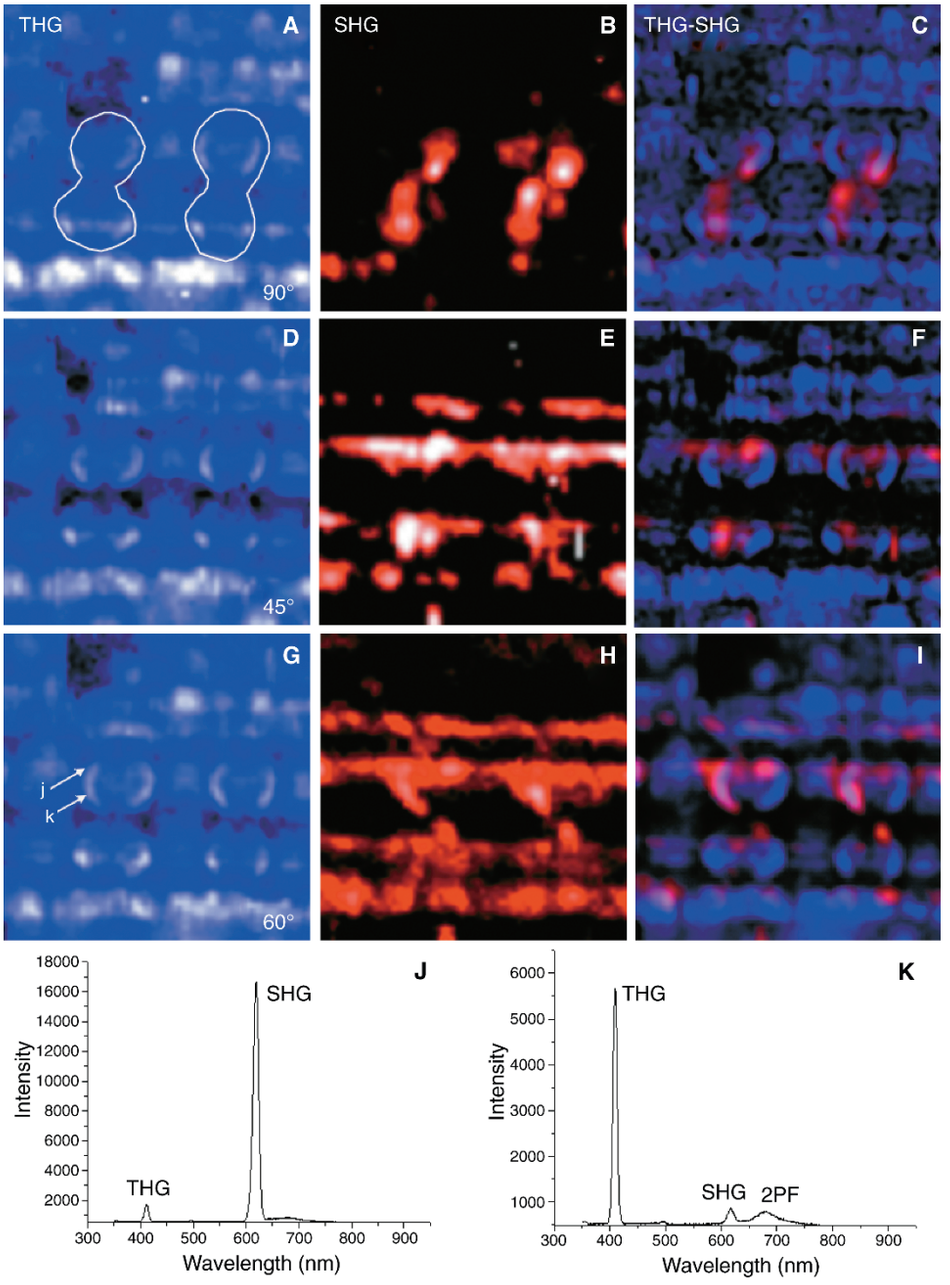

FIGURE 40.23. Polarization dependence of the SHG signal. (A–C) Ninety-degree polarization; (D–F) 45° polarization; and (G–I) 60° polarization. Note that the change of illumination polarization has little effect to the THG image, but the SHG signal does show polarization dependence. The spectra at the bottom of this figure (J, K) were obtained at the points labeled in (G).

SUMMARY

Highly organized nanoperiodic structures in biological samples exhibit strong SHG activity resembling that of nonlinear photonic crystals and thus they can be treated as nonlinear biophotonic crystals. Many biological structures, such as microfibrils in cell walls, alternating crystalline lamellae in starch granules, cuticular papillae on the leaf surface, crystalline myosin and actin nanofilaments in the myofibrils of skeletal and cardiac muscle, thylakoid membranes and grana in chloroplasts, and microtubules in both the cytoskeleton and the mitotic apparatus, all exhibit strong biophotonic effects. Many of the birefringent structures found in biological specimens also exhibit SHG properties (Table 40.3). The relative locations and orientation of these biophotonic structures can be examined using SHG microscopy, while optical interfaces and the functional molecules can be separately located by THG and 2PF contrast. In contrast to single- and multi-photon absorption, harmonic generation involves only virtual states and does not involve energy deposition. The harmonic signals allow 3D structural visualization with minimal or no additional preparation of the sample. Meanwhile, 2PF imaging modes can be added to monitor multiple molecular probes in living cells and tissues, such as those

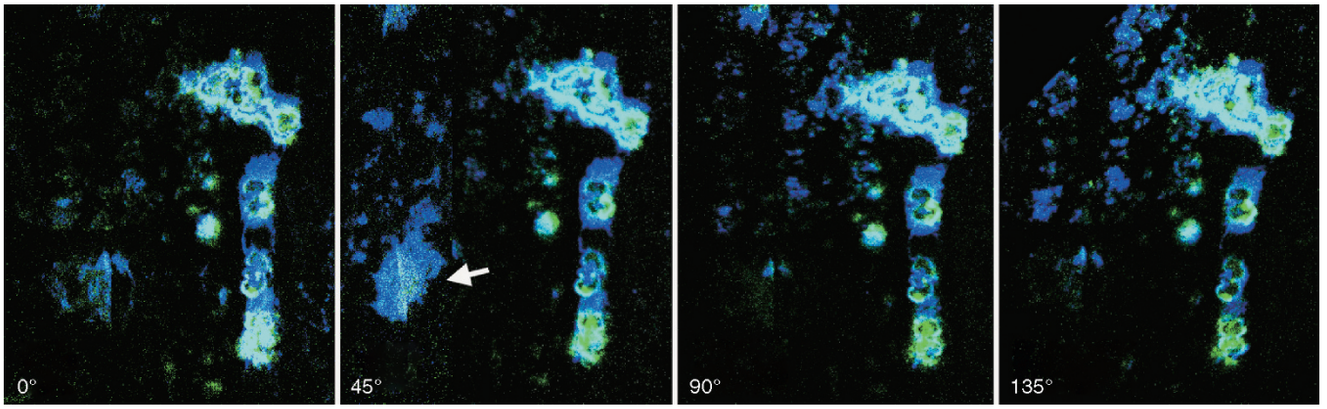

FIGURE 40.24. Isolated phytoliths, illuminated using different polarization directions. Note that the SHG (green) and THG (blue) signals vary little with different illumination conditions. The THG patch (*arrow*) in the 45° image may be the result of focal drift bringing the underlying cuticular surface into focus.

composed of transformed cells or taken from transgenic organisms. Multi-modal microscopy can provide a powerful tool for investigating the dynamics of structure–function relationships at the molecular and subcellular levels.

ACKNOWLEDGMENTS

Most of the images presented in this chapter come from research performed at the Graduate Institute of Electro-Optical Engineering and Department of Electrical Engineering, National Taiwan University, Taipei, Taiwan, by a number of researchers: I. H. Chen, T.-M. Liu, Mei-Hsin Chen, Szu-Yu Chen, and Shi-Wei Chu. Most of the biological work was done by Huai-Jen Tsai and Chung-Yung Lin of the Graduate Institute of Molecular and Cell Biology, National Taiwan University, and B.-L. Lin, S.-P. Lee of Molecular and Cell Biology Division, Development Center for Biotechnology, Taipei. The transmission spectroscopy was done by M.-X. Kuo, D.-J. Lin, and H.-L. Liu. Thanks are also due to Nick White, Sir William Dunn School of Pathology, University of Oxford for his help editing the proofs.

REFERENCES

Anderson, R.R., and Parrish, J.A., 1981, The optics of human skin, *J. Invest. Dermatol.* 77:13–19.

Barad, Y., Eisenberg, E., Horowitz, M., and Silberberg, Y., 1997, Nonlinear scanning laser microscopy by third harmonic generation, *Appl. Phys. Lett.* 70:922–924.

Berger, V., 1998, Nonlinear photonic crystals, *Phys. Rev. Lett.* 81:4136–4139.

Birge, R.R., Fleitz, P.A., Lawrence, A.F., Masthay, M.A., and Zhang, C.F., 1990, Nonlinear optical properties of bacteriorhodopsin: Assignment of second order hyperpolarizabilities of randomly oriented systems using two-photon spectroscopy, *Mol. Cryst. Liq. Cryst.* 189:107–122.

Bouma, B.E., Tearney, G.J., Bilinsky, I.P., Golubovic, B., and Fujimoto, J.G., 1996, Self-phase-modulated Kerr-lens mode-locked Cr:Forsterite laser source for optical coherence tomography, *Opt. Lett.* 21:1839.

Broderick, N.G.R., Ross, G.W., Offerhaus, H.L., Richardson, D.J., and Hanna, D.C., 2000, Hexagonally poled lithium niobate: A two-dimensional nonlinear photonic crystal, *Phys. Rev. Lett.* 84:4345–4348.

Campagnola, P.J., Wei, M.-D., Lewis, A., and Loew, L.M., 1999, High resolution nonlinear optical imaging of live cells by second harmonc generation, *Biophys. J.* 77:3341–3349.

Chen, I.-H., Chu, S.-W., Sun, C.-K., Cheng, P.C., and Lin, B.L., 2002, Wavelength dependent cell damages in multi-photon confocal microscopy, *Opt. Quantum Electron*. 34:1251–1266.

Cheng, P.C., 1987, Sample preparation for X-ray imaging and examples of biological X-ray images, In: *X-Ray Microscopy-Instrumentation and Biological Applications* (P.C. Cheng and G.J. Jan, eds.), Springer-Verlag, Berlin, pp. 289–310.

Cheng, P.C., and Lin, T.H., 1990, The use of computer-controlled substage folding optics to enhance signal strength in fluorescent confocal microscopy, *Trans. Royal Microscop. Soc.* 1:459–462.

Cheng, P.C., Lin, B.L., Kao, F.J., Gu, M., Xu, M.-G., Gan, X., Huang, M.-K., and Wang, Y.-S., 2001a, Multi-photon fluorescence microscopy — The response of plant cells to high intensity illumination, *Micron* 32:661–669.

Cheng, P.C., Newberry, S.P., Kim, H.G., Wittman, M.D., and Hwang, I.-S., 1990, X-ray contact microradiography and shadow projection microscopy, In: *Modern Microscopy* (P. Duke and A. Michette, eds.), Plenum Press, New York, pp. 87–117.

Cheng, P.C., Pan, S.J., Shih, A., Kim, K.S., Liou, W.S., and Park, M.S., 1998, Highly efficient upconverters for multiphoton fluorescence microscopy, *J. Microsc.* 189:199–212.

Cheng, P.C., Sun, C.-K., Kao, F.-J., Lin, B.-L., and Chu, S.-W., 2001b, Nonlinear multi-modality spectro-microscopy: Multiphoton fluorescence, SHG and THG of biological specimen, *SPIE Proc.* 4262:98–103.

Cheng, P.C., Sun, C.K., Lin, B.L., and Chu, S.W., 2002, Bio-photonic crystal: SHG imaging. *Maize Genetics Cooperation Newsletter* 76:8–9.

Chu, S.W., Chen, I.S., Li, T.M., Lin, B.L., Cheng, P.C., and Sun, C.K., 2001, Multi-modality nonlinear spectral microscopy based on a femtosecond Cr:Forsterite laser, *Opt. Lett.* 26:1909–1911.

Chu, S.-W., Chen, I.-S., Liu, T.-M., Sun, C.-K., Lee, S.-P., Lin, B.-L., Cheng, P.-C., Kuo, M.-X., Lin, D.-J., and Liu, H.-L., 2002, Nonlinear bio-photonic crystal effects revealed with multi-modal nonlinear microscopy, *J. Microsc.* 208:190–200.

Chu, S.-W., Chen, S.-Y., Tsai, T.-H., Liu, T.-M., Lin, C.-Y., Tsai, H.J., and Sun, C.-K., 2003a, *In vivo* developmental biology study using noninvasive multi-harmonic generation microscopy, *Opt. Express* 11:3093–3099.

Chu, S.W., Liu, T.M., Sun, C.K., Lin, C.Y., and Tsai, H.J., 2003b, Real-time second-harmonic-generation microscopy on a 2-GHz repetition rate Ti:Sapphire laser, *Opt. Express* 8:933–938.

Chu, S.-W., Chen, S.-Y., Chern, G.-W., Tsai, T.-H., Chen, Y.-C., Lin, B.-L., and Sun, C.-K., 2004, Studies of (2)/(3) tensors in submicron-scaled biotissues by polarization harmonics optical microscopy, *Biophys. J.* 86:3914–3922.

Clays, K., Elshocht, S.V., Chi, M., Lepoudre, E., and Persoons, A., 2001, Bacteriorhodopsin: A natural, efficient (nonlinear) photonic crystal, *J. Opt. Soc. Am. B* 18:1474–1482.

Denk, W., Strickler, J.H., and Webb, W.W., 1990, Two-photon laser scanning fluorescence microscopy, *Science* 248:73–76.

Dumeige, Y., Vidakovic, P., Sauvage, S., Levenson, J.A., Sibilla, C., Centini, M., D'Aguanno, G., and Scalora, M., 2001, Enhancement of second-harmonic generation in a one-dimensional semiconductor photonic band gap, *Appl. Phys. Lett.* 78:3021–3023.

Freund, I., Deutsch, M., and Sprecher, A., 1986, Connective tissue polarity: Optical second-harmonic microscopy, crossed-beam summation, and small-angle scattering in rat-tail tendon, *Biophys. J.* 50:693–712.

Gallant, D.J., Bouchet, B., and Baldwin, P.M., 1997, Microscopy of starch: Evidence of a new level of granule organization, *Carbohydrate Polym.* 32:177–191.

Gannaway, J.N., and Sheppard, C.J.R., 1978, Second-harmonic imaging in the scanning optical microscope, *Opt. Quantum Electron.* 10:435–439.

Gunning, B., and Steer, M., 1996, *Plant Cell Biology: Structure and Function*, Jones and Bartlett Publishers, Sudbury, Massachusetts, p. 21.

Gu, X., Makarov, M., Ding, Y.J., Khurgin, J.B., and Risk, W.P., 1999, Backward second-harmonic and third-harmonic generation in a periodically poled potassium titanyl phosphate waveguide, *Opt. Lett*. 24:127.

Guo, Y., Ho, P.P., Tirksliunas, A., Liu, F., and Alfano, R.R., 1997, Optical harmonic generation from animal tissues by the use of picosecond and femtosecond laser pulses, *Opt. Lett*. 22:1323–1325.

Hodson, M.J., and Sangster, A.G., 1989, Silica deposition in the inflorescence bracts of wheat (Triticum aestivum). II X-ray microanalysis and backscattered electron imaging, *Can. J. Botany* 67:281–287.

Kao, F.J., Huang, M.K., Wang, Y.S., Hung, S.L., Lee, M.K., Sun, C.K., and Cheng, P.C., 2000, Two-photon optical-beam-induced current microscopy of indium gallium nitride light emitting diodes, *SPIE Proc.* 4082:92–98.

Konig, K.H., Liang, M., Berns, W., and Tromberg, B.J., 1995, Cell damage by near-IR microbeams, *Nature* 377:20–21.

Lin, B.-L., Cheng, P.C., and Sun, C.-K., 2001, Optical density of leaf, *Maize Genetics Cooperation Newsletter,* 75:61–62.

Liu, T.M., Chu, S.W., Sun, C.K., Lin, B.L., Cheng, P.C., and Johnson, I., 2001, Multiphoton confocal microscopy using a femtosecond Cr:Forsterite laser, *Scanning* 23:249–254.

Moreaux, E., Sandre, O., and Mertz, J., 2000a, Membrane imaging by second-harmonic generation microscopy, *J. Opt. Soc. Am. B*. 17:1685–1694.

Moreaux, L., Sandre, O., Blanchard-Desce, M., and Mertz, J., 2000b, Membrane imaging by simultaneous second-harmonic generation and two-photon microscopy, *Opt. Lett.* 25:320–322.

Muller, M., Squier, J., Wilson, K.R., and Brakenhoff, G.J., 1998, 3D microscopy of transparent objects using third-harmonic generation, *J. Microsc*. 191:266–274.

Oldenbourg, R., and Mei, G., 1995, A new polarized light microscope with precision universal compensator, *J. Microsc.* 180:140–147.

Peleg, G., Lewis, A., Linial, M., and Loew, L.M., 1999, Nonlinear optical measurement of membrane potential around single molecules at selected cellular sites, *Proc. Natl. Acad. Sci. USA* 96:6700–6704.

Peter, H.R., Ray, F.E., and Susan, E.E., 1992, *Biology of Plants*, Worth Publishers, New York, p. 36.

Roth, S., and Freund, I., 1979, Second harmonic-generation in collagen, *J. Chem. Phys.* 70:1637–1643.

Roth, S., and Freund, I., 1981, Optical second-harmonic scattering in rat-tail tendon, *Biopolymers* 20:1271–1290.

Shen, Y.R., 1989, Surface properties probed by 2nd harmonic and sum frequency generation, *Nature* 337:519–525.

Sheppard, C.J.R., and Shotton, D.M., 1997, *Confocal Laser Scanning Microscopy,* BIOS Scientific Publisher, Oxford, United Kingdom.

Stoller, P., Kim, B.M., Rubenchik, A.M., Reiser, K.M., and Da Silva, L.B., 2002a, Polarization-dependent optical second-harmonic imaging of a rat-tail tendon, *J. Biomed. Opt*. 7:205–214.

Stoller, P., Reiser, K.M., Celliers, P.M., and Rubenchik, A.M., 2002b, Polarization-modulated second harmonic generation in collagen, *Biophys. J*. 82:3330–3342.

Sun, C.K., 2005, Higher Harmonic generation biopsy, *Focus on Microscopy 2005*, Jena, Germany.

Sun, C.-K., Chen, C.-C., Chu, S.-W., Tsai, T.-H., Chen, Y.-C., and Lin, B.-L., 2003, Multiharmonic generation biopsy of skin, *Opt. Lett*. 28:2488–2490.

Sun, C.-K., Chu, S.-W., and Liu, T.-M., 2002, High frame-rate second-harmonic generation micoscopy based on a 2 GHz Ti: sapphire laser, *Proc. OSA* paper TuH4.

Sun, C.-K., Chu, S.-W., Chen, S.-Y., Tsai, T.-H., Liu, T.-M., Lin, C.-Y., and Tsai, H.-J., 2004, Higher harmonic generation microscopy for developmental biology, *J. Struct. Biol*. 147:19–30.

Sun C.-K., Chu, S.-W., Tai, S.P., Keller, S., Abare, A., Mishira, U.K., and DenBaars, S.P., 2001, Mapping piezoelectric-field distribution in gallium nitride with scanning second-harmonic generation microscopy, *Scanning* 23:182–192.

Sun, C.-K., Chu, S.-W., Tai, S.-P., Keller, S., Mishra, U.K., and DenBaars, S.P., 2000, Scanning second-harmonic-generation and third-harmonic-generation microscopy of GaN, *Appl. Phys. Lett.* 77:2331–2333.

Williams, R.M., Zipfel, W.R., and Webb, W.W., 2005, Interpreting second-harmonic generation images of collagen I fibrils, *Biophys. J.* 88:1377–1386.

Zhao, T., Chen, Z.-H., Chen, F., Shi, W.-S., Lu, H.-B., and Yang, G.-Z., 1999, Enhancement of second-harmonic generation in $BaTiO_3/SrTiO_3$ superlattices, *Phys. Rev. B* 60:1697–1700.

Zipfel, W.R., Williams, R.M., Christie, R., Nikitin, A.Y., Hyman, B.T., and Webb, W.W., 2003, Live tissue intrinsic emission microscopy using multiphoton excited intrinsic fluorescence and second harmonic generation, *Proc. Natl. Acad. Sci. USA* 100:7075–7080.